



1 **Causes of interannual variability of tropospheric ozone**  
2 **over the Southern Ocean**

3 Junhua Liu<sup>1,2</sup>, Jose M. Rodriguez<sup>2</sup>, Stephen D. Steenrod<sup>1,2</sup>, Anne R. Douglass<sup>2</sup>, Jennifer  
4 A. Logan<sup>3</sup>, Mark Olsen<sup>2,4</sup>, Krzysztof Wargan<sup>2,5</sup>, Jerald Ziemke<sup>2,4</sup>

5 <sup>1</sup>Universities Space Research Association (USRA), GESTAR, Columbia, MD, USA

6 <sup>2</sup>NASA Goddard Space Flight Center, Greenbelt, Maryland, USA

7 <sup>3</sup> School of Engineering and Applied Sciences, Harvard University, Cambridge, MA,  
8 USA

9 <sup>4</sup> Morgan State University, Baltimore, Maryland, USA

10 <sup>5</sup> Science Systems and Applications, Inc., Lanham, MD, USA

11

12 *Correspondence to:* Junhua Liu (junhua.liu@nasa.gov)



13 **Abstract.**

14 We examine the relative contribution of processes controlling the interannual variability  
15 (IAV) of tropospheric ozone over four sub-regions of the southern hemispheric  
16 tropospheric ozone maximum (SHTOM) over a twenty-year period. Our study is based  
17 on hindcast simulations from the National Aeronautics and Space Administration Global  
18 Modeling Initiative – Chemistry transport model (NASA GMI-CTM) of tropospheric and  
19 stratospheric chemistry, driven by assimilated Modern Era Retrospective-Analysis for  
20 Research and Applications (MERRA) meteorological fields. Our analysis shows that over  
21 SHTOM region, the IAV of the stratospheric contribution is the most important factor  
22 driving the IAV of upper tropospheric ozone (270 hPa), where ozone has a strong  
23 radiative effect. Over the south Atlantic region, the contribution from surface emissions  
24 to the IAV of ozone exceeds that from stratospheric input at and below 430 hPa. Over the  
25 south Indian Ocean, the IAV of stratospheric ozone makes the largest contribution to the  
26 IAV of ozone with little or no influence from surface emissions at 270 hPa and 430 hPa  
27 in austral winter. Over the tropical south Atlantic region, the contribution from IAV of  
28 stratospheric input dominates in austral winter at 270 hPa and drops to less than half but  
29 is still significant at 430 hPa. Emission contributions are not significant at these two  
30 levels, even during September. The IAV of lightning over this region also contributes to  
31 the IAV of ozone in September and December. Over the tropical southeastern Pacific, the  
32 contribution of the IAV of stratospheric input is significant at 270 hPa and 430 hPa in  
33 austral winter, and emissions have little influence.

34 **1 Introduction**

35 Tropospheric ozone plays a critical role in controlling the oxidative capacity of the  
36 troposphere through its photolysis in the presence of water vapor, generating hydroxyl  
37 radical (OH), the main atmospheric oxidant (e.g., Logan et al., 1981). It contributes to  
38 smog and is harmful to human and ecosystem health near the surface. It acts as a  
39 greenhouse gas in the upper troposphere (Lacis et al., 1990) and affects the radiative  
40 forcing of the climate system. Tropospheric ozone is produced by photochemical  
41 oxidation of CO and volatile organic compounds (VOCs) in the presence of nitrogen



42 oxides (NO<sub>x</sub>) (e.g., Logan et al., 1981). Downward transport of ozone from the  
43 stratosphere is also an important source of tropospheric ozone (e.g., Danielsen, 1968;  
44 Stohl et al., 2003). Deep convection and long-range transport of ozone and its precursors  
45 also modulate the tropospheric O<sub>3</sub> distributions (e.g., Chandra et al., 2009; Oman et al.,  
46 2011).

47 Our study is motivated by the existence of tropospheric ozone maximum over tropical  
48 and subtropical southern hemisphere as seen both in model simulations and GMAO  
49 assimilated ozone product derived from OMI/MLS satellite measurements (Figure 1).  
50 Although in the southern hemisphere tropospheric air is relatively “clean” and less  
51 polluted compared with the Northern Hemisphere, this tropospheric ozone column  
52 maximum reaches as high as 35DU and is comparable to the typical northern mid-latitude  
53 values of 30DU. The elevated tropospheric ozone column is centered over the south  
54 Atlantic from the equator to 30°S, and is part of the well-known tropical wave-one  
55 pattern first noted in observations made by the Nimbus 7 Total Ozone Mapping  
56 Spectrometer (TOMS) (e.g., Fishman et al., 1990; Ziemke et al., 1996). This ozone  
57 maximum extends westward to South America and the tropical southeastern Pacific,  
58 southeastward to southern Africa, south Indian Ocean along the latitude band of 30°S-  
59 45°S, and is a dominant global feature (Thompson et al., 2003; Sauvage et al., 2007).  
60 This elevated ozone region exists year-around, with a seasonal maximum in August -  
61 October, and a seasonal minimum in April - May.

62 This study provides an examination of the relative contributions of the factors that control  
63 the interannual variations of the southern hemisphere tropospheric ozone maximum over  
64 a twenty-year period. Prior studies have examined the processes that produce the  
65 southern hemisphere tropospheric ozone maximum (SHTOM), but consider only short  
66 periods or are limited in spatial scale. These studies concluded that horizontal and vertical  
67 transport of ozone precursors from regions of biomass burning (e.g., Jacob et al., 1996;  
68 Pickering et al., 1996; Thompson et al., 1996; Jenkins and Ryu, 2004a; Sauvage et al.,  
69 2006; Jourdain et al., 2007; Thouret et al., 2009), lightning NO<sub>x</sub> (Martin et al., 2002;  
70 Jenkins and Ryu, 2004b; Kim et al., 2013; Tocquer et al., 2015) and stratospheric  
71 intrusions (Weller et al., 1996) all contribute to this tropospheric ozone column  
72 maximum. However, changes of the relative contributions of these factors to tropospheric



73 ozone on inter-annual time scale over this region have not been examined in detail.  
74 Studies considering tropospheric ozone interannual variability have not focused on the  
75 SHTOM region. Zeng et al. (2005) used a combined climate/chemistry model to evaluate  
76 the ENSO effects on the interannual variability of tropospheric ozone. Their study  
77 concludes that STE variation induced by ENSO is one important factor driving the IAV  
78 of the global mean of tropospheric ozone. Voulgarakis et al. (2010) examined the  
79 drivers of interannual variability of the global tropospheric ozone using the p-TOMCAT  
80 tropospheric chemistry transport model (CTM). Their study shows that changing  
81 transport including the STE is important in determining the IAV of tropospheric ozone.  
82 The influence of emissions is confined to areas of intense burning on the interannual  
83 timescale. Murray et al. (2013) examined the effects of lightning on the IAV in the  
84 tropical tropospheric ozone column based on the GEOS-Chem CTM with IAV in tropical  
85 lightning constrained by satellite observations from Lightning Imaging Sensors (LIS).  
86 Their study finds that lightning plays an important role in driving the IAV of tropical  
87 tropospheric ozone column, especially over East Africa, central Brazil, and in continental  
88 outflow in the eastern Pacific and the Atlantic, but their model does not reproduce the  
89 IAV in TCO except in East Africa and central Brazil. Liu et al. (2016) analyzed  
90 simulations from a global chemistry and transport model to show that the IAV in the  
91 stratospheric contribution significantly affects the IAV of upper tropospheric ozone at the  
92 SHADOZ station over Reunion (21°S). In this study, we focus on the SHTOM region  
93 and quantify the relative contributions of several factors to the tropospheric ozone  
94 interannual variability during the past twenty years. We examine the horizontal and  
95 vertical variations of these contributions by separating the SHTOM into four subregions  
96 and comparing their IAVs at two selected levels (270 hPa and 430 hPa). This analysis  
97 distinguishes between anthropogenic and natural sources on the IAV of the tropospheric  
98 ozone and their contributions to the radiative forcing changes.

99 In this study, we use a global chemistry transport model to identify the processes  
100 impacting observed interannual variability of the tropospheric ozone column maximum in  
101 southern hemisphere. We examine the model sensitivity of tropospheric ozone to  
102 different ozone sources through the use of multiple linear regression. We include  
103 stratospheric input and emissions as two major predictor variables in our regression. In



104 our GMI-CTM, the global total of  $\text{NO}_x$  from lightning is fixed at 5.0 TgN/yr. The  
105 regional  $\text{NO}_x$  emission from lightning is coupled to the deep convective transport and  
106 mixing in the model varies from year to year. We include the lightning  $\text{NO}_x$  as the third  
107 factor in our regression model over the tropical south Atlantic region, where ozone is  
108 sensitive to the IAV of lightning  $\text{NO}_x$  as found in Murray et al (2013). In our multiple  
109 linear regression, a regression coefficient that is significantly different from zero at the  
110 95% confidence level implies that the corresponding process contributes significantly to  
111 the variation of simulated ozone. We thereby quantify their relative contributions to the  
112 interannual variability of tropospheric ozone. Our study focuses on austral winter season  
113 when the subtropical jet related stratosphere - troposphere exchange reaches the seasonal  
114 maximum (Karoly et al., 1998; Bals-Elsholz et al., 2001; Nakamura and Shimpo, 2004).  
115 Southern hemisphere biomass burning (e.g., Liu et al., 2010; 2013) also reaches the  
116 maximum during this season.

117 Section 2 briefly describes the model and simulations, including the standard chemistry  
118 simulation, the stratospheric  $\text{O}_3$  tracer simulation, and the tagged CO simulation. It also  
119 describes GEOS-5 ozone assimilation, as the assimilated fields are used to evaluate  
120 model performance over the southern hemisphere extra-tropics and tropics as discussed  
121 in the first part of section 3. The second part of section 3 presents a diagnostic study of  
122 controlling factors, including stratosphere input, surface emissions and lightning, on the  
123 tropospheric ozone IAV relying on a series of hindcast simulations from 1992 to 2011.  
124 Section 4 is a summary and conclusion.

## 125 **2 Model and Data**

### 126 **2.1 Model**

127 We used the Global Modeling Initiative chemical transport model (GMI-CTM) (Duncan  
128 et al., 2007; Strahan et al., 2007), driven by MERRA reanalysis meteorology (Rienecker  
129 et al., 2011, [http:// gmao.gsfc.nasa.gov/research/merra/](http://gmao.gsfc.nasa.gov/research/merra/)). The native resolution of the  
130 MERRA field is  $0.67^\circ \times 0.5^\circ$  with 72 vertical levels; we regrid it to  $2^\circ \times 2.5^\circ$  for input to  
131 the GMI-CTM simulations in this study.



132 The chemical mechanism used in GMI-CTM represents stratospheric and tropospheric  
133 chemistry with offline aerosols input from GOCART model simulations (Chin et al.,  
134 2002). The GMI-CTM hindcast simulation has been used and compared to observations  
135 in many recent studies. Strahan et al. (2013) showed excellent agreement between  
136 simulated and MLS ozone profiles in the Arctic lower stratosphere and. Liu et al. (2016)  
137 shows the GMI-CTM hindcast and ozonesonde agree very well on the annual cycles and  
138 IAV over Reunion from lower troposphere to the upper troposphere. Strode et al. (2015)  
139 shows that the GMI-CTM hindcast reproduces the seasonal cycle and IAV of observed  
140 surface ozone over United States from Environmental Protection Agency (EPA)'s Clean  
141 Air Status and Trends Network (CASTNET).

142 The sources of emissions in the GMI-CTM standard simulation are summarized in the  
143 recent study of Strode et al. (2015). Besides the standard simulation, we also carry out a  
144 control run with constant emissions fixed at the year 2000 levels to quantify effects of  
145 emission IAV on ozone IAV.

146 The lightning parameterization in the model follows the scheme described by Allen et al  
147 (2010) and the emissions of lightning  $\text{NO}_x$  are calculated online. The global total of  $\text{NO}_x$   
148 from lightning is fixed every year but varies spatially.

149 Methane mixing ratios are specified in the two lowest model levels, using time dependent  
150 zonal means from National Oceanic and Atmospheric Administration / Global  
151 Monitoring Division (NOAA/GMD). Other long-lived source gases important in the  
152 stratosphere, such as  $\text{N}_2\text{O}$ , CFCs, halocarbons are prescribed at the two lowest model  
153 levels following the A2 scenario by (WMO, 2014). Stratospheric aerosol  
154 distributions/trends are from International Global Atmospheric Chemistry/Stratospheric  
155 Processes And their Role in Climate (IGAC/SPARC) and have IAV (Eyring et al., 2013).

156 The model includes a stratospheric  $\text{O}_3$  tracer (Strat $\text{O}_3$ ). The Strat $\text{O}_3$  is defined relative to a  
157 dynamically varying tropopause tracer (e90) (Prather et al., 2011). This artificial tracer is  
158 set to a uniform mixing ratio (100 ppb) at the surface with 90 days e-folding lifetime. In  
159 our simulation, the e90 tropopause value is 90 ppb. The Strat $\text{O}_3$  tracer is set equal to  $\text{O}_3$  in  
160 the stratosphere and is removed in the troposphere with the same loss frequency  
161 (chemistry and deposition) archived from daily output of the standard chemistry model  
162 simulation with yearly-varied emission in this study. Using the Strat $\text{O}_3$  tracer allows



163 quantification of O<sub>3</sub> of stratospheric origin in the troposphere at a given location and  
164 time. This approach has also been adopted in the high resolution GFDL AM3 model (Lin  
165 et al., 2012).

166 In this study, we also conducted a tagged CO simulation to examine the emission sources  
167 during the same period as the full chemistry simulation. The tagged CO simulation has  
168 horizontal resolution of 1°x1.25°. The primary chemical loss of CO is through reactions  
169 with OH radicals, which are archived from the respective standard chemistry simulation  
170 with yearly-varied emissions. The chemical production and loss rates of CO in the  
171 stratosphere were archived from the respective standard chemistry simulations.

## 172 **2.2 GMAO GEOS-5 Ozone Assimilation**

173 We used assimilated tropospheric ozone to evaluate model performance. This assimilated  
174 dataset is produced by ingesting OMI v8.5 total column ozone and MLS v3.3 ozone  
175 profiles into a version of the Goddard Earth Observing System, Version 5 (GEOS-5) data  
176 assimilation system (Rienecker et al., 2011). No ozonesonde data are used in the  
177 assimilation. Wargan et al. (2015) provides details of the GEOS-5.7.2 assimilation  
178 system, which for this application is produced with 2° x 2.5° horizontal resolution and  
179 with 72 vertical layers between the surface and 0.01 hPa. For the troposphere, the  
180 assimilation only applies a dry deposition mechanism at the surface without any chemical  
181 production or loss. This algorithm works since the ozone lifetime is much longer than the  
182 six-hour analysis time on which the background field is corrected by observations.  
183 Ziemke et al. (2014) evaluated the tropospheric ozone profiles derived from three  
184 strategies based on OMI and MLS measurements, including this GEOS-5 assimilation,  
185 trajectory mapping and direct profile retrieval using residual method, with ozonesonde  
186 observations and GMI model simulations. They show that the ozone product (500 hPa to  
187 tropopause) from the GEOS-5 assimilation is the most realistic. Wargan et al. (2015) also  
188 demonstrate that the ozone between 500 hPa and the tropopause from GEOS-5  
189 assimilation is in good agreement with independent observations from ozonesondes. The  
190 assimilation applies the OMI averaging kernels in the troposphere, but the weight of OMI  
191 kernels decreases sharply below 500 hPa (Personal communication with K. Wargan).  
192 Considering that in the lower troposphere there is no direct observational constraint in



193 the analysis, we use ozone mixing ratio at 270 hPa and 430 hPa as well as partial column  
194 ozone integrated from 500 hPa to the tropopause from GEOS-5 assimilation as a  
195 reference value to evaluate our GMI model simulation. To compare the GEOS-5  
196 assimilated tropospheric partial column above 500 hPa with GMI-CTM ozone  
197 simulation, we use the same tropopause as defined by the lower of the 3.5 potential  
198 vorticity units (PVU) isosurface and the 380 K isentropic surface.

## 199 **3 Results**

### 200 **3.1 Temporal and spatial distribution of SHTOM in GMI-CTM and GMAO GEOS-** 201 **5 assimilated ozone product**

202 Figure 1 shows the spatial pattern of southern hemispheric partial column ozone (from  
203 500 hPa to the tropopause) in four seasons averaged over 2005 to 2011 from the GMAO  
204 GEOS-5 assimilated dataset and the GMI-CTM hindcast simulations. To account for a  
205 low bias in the GEOS-5 ozone product (Wargan et al., 2015), we added 2.5 DU to the  
206 assimilated column in the tropics (0-30°S). The GMI-CTM simulation reproduces the  
207 seasonality and spatial distribution of southern hemispheric ozone maximum as shown in  
208 GEOS-5 assimilated product with a) the elevated ozone centered over the Atlantic Ocean  
209 from the equator to 40°S; b) the ozone maximum extending southeastward to southern  
210 Africa and the Indian Ocean in the latitude band of 30°S-45°S; c) the relatively weaker  
211 enhancement extending westward to South America and the tropical southeastern Pacific.  
212 The elevated ozone maximum is strongest in austral winter-spring and weakest in austral  
213 fall. Both GMI-CTM and GEOS-5 assimilation show the very low tropospheric ozone  
214 over the western Pacific and the tropical eastern Indian Ocean, where the ozone - poor  
215 marine boundary layer air is lifted into the upper troposphere (Folkins et al., 2002;  
216 Solomon et al., 2005).

### 217 **3.2 Subregions of SHTOM**

218 The tropospheric ozone distribution depends on the advection and mixing, their proximity  
219 to the polluted area, and descent of ozone-rich air from the stratosphere. We show in  
220 Figure 2 the maps of simulated  $O_3$  and  $StratO_3/O_3$  at 430 hPa averaged over 1992 to 2011



221 in September, when the southern hemisphere biomass burning peaks. The  $\text{StratO}_3/\text{O}_3$  ratio  
222 represents fraction of tropospheric ozone from stratosphere and is used to identify the  
223 regions with distinct stratospheric input. Differences in the spatial patterns of the  
224 maximum/minimum in ozone mixing ratio and  $\text{StratO}_3/\text{O}_3$  ratio identifies regions where  
225 ozone is affected by factors other than the stratospheric input.

226 The region with minimum stratospheric ozone contribution occurs along the equator. It  
227 extends southward to approximately  $10^\circ\text{S}$  over South America and further south to  
228 approximately  $15^\circ\text{S}$  over the Indian Ocean and the Maritime Continents. In the tropics,  
229 the southward extension of regions with minimum stratospheric ozone contribution  
230 shows strong meridional variation that is closely related to the Walker Circulation. In this  
231 tropical meridional circulation air rises over the Maritime Continents (together with deep  
232 convection) and descends over the eastern Pacific (Bjerknes, 1969). Similar meridional  
233 circulation is found over the Atlantic with rising due to radiative heating over tropical  
234 Africa and South America and sinking due to radiative cooling over the tropical Atlantic  
235 (Julian and Chervin, 1978). The longitudinal variation of ozone at 430 hPa in the tropics  
236 is in agreement with the changes of  $\text{StratO}_3/\text{O}_3$ , showing ozone minimum over South  
237 America, tropical Africa and Maritime Continents. Within the Atlantic, despite of the  
238 smaller stratospheric contribution, the tropics have higher ozone mixing ratio ( $>80$  ppb)  
239 than the subtropics at 430 hPa, and other sources must also contribute to the ozone  
240 maximum over tropical south Atlantic. Ozone over the tropical southeastern Pacific is  
241 also slightly elevated. The maximum stratospheric influence is found over the Southern  
242 Ocean centered on  $30^\circ\text{S}$ , co-located with the tropospheric  $\text{O}_3$  maximum over these  
243 regions. Both ozone and  $\text{StratO}_3/\text{O}_3$  over the subtropics show strong longitudinal  
244 variations, with the co-located maxima over the south Indian Ocean. The ozone minimum  
245 at 430 hPa at  $30^\circ\text{S}$  occurs over the eastern Pacific region, while the minimum  
246 contribution of the stratospheric input is over the south Atlantic region. Given the spatial  
247 variations of the maximum/minimum in  $\text{StratO}_3/\text{O}_3$  ratio and ozone mixing ratio, we  
248 separate the southern hemispheric ozone maximum into four sub-regions: 1) Tropical  
249 southeastern Pacific ( $0\text{--}20^\circ\text{S}$ ,  $150^\circ\text{W}\text{--}60^\circ\text{W}$ ); 2) Tropical South Atlantic ( $0\text{--}15^\circ\text{S}$ ,  $60^\circ\text{W}\text{--}$   
250  $40^\circ\text{E}$ ); 3) Subtropical South Atlantic ( $15^\circ\text{S}\text{--}45^\circ\text{S}$ ,  $60^\circ\text{W}\text{--}40^\circ\text{E}$ ); 4) Subtropical South  
251 Indian Ocean ( $15^\circ\text{S}\text{--}45^\circ\text{S}$ ,  $40^\circ\text{E}\text{--}150^\circ\text{E}$ ). We examine and quantify the relative roles of



252 dynamics and chemistry on the IAV of tropospheric ozone variations over these selected  
253 regions during the past twenty years.

254 Figure 3 compares the anomalies of modeled and assimilated tropospheric ozone mixing  
255 ratio at 270 hPa and 430 hPa as well as the anomalies of corresponding upper  
256 tropospheric ozone columns (UTOC, integrated from 500 hPa to the tropopause) over  
257 two tropical sub-regions (tropical south Atlantic and tropical southeastern Pacific) from  
258 2005 to 2011. The anomalies are calculated by removing the monthly mean averaged  
259 from 2005 to 2011. The short time scale variations in the model simulation tend to be  
260 greater compared to that in the assimilated ozone products, especially over the tropical  
261 south Atlantic region. But in general, the GMI-CTM hindcast simulation captures the  
262 assimilated IAV of the tropospheric ozone at these two levels as well as for the UTOC.  
263 Over the tropical south Atlantic, the modeled IAV agrees with the phase changes of  
264 assimilated ozone IAV but the simulation overestimates the assimilated ozone maximum  
265 in 2010 and underestimates the assimilated minima in 2007 and 2011 at both levels. Over  
266 the tropical southeastern Pacific, the IAV is influenced by ENSO related changes in  
267 dynamics (e.g., Ziemke et al., 2010; Oman et al., 2013; 2011). The simulation matches  
268 much of the assimilated IAV, showing high ozone anomalies after 2005, 2010 La Nina  
269 year and negative ozone anomalies after strong El Niño year in 2009. However, during  
270 October 2006 to January 2007, the simulation shows a pronounced ozone peak, especially  
271 at 270 hPa, which is not seen in the assimilated ozone. Logan et al. (2008) examined  
272 interannual variations of tropospheric ozone profiles in October-December between 2005  
273 and 2006 based on the satellite observations from Tropospheric Emission Spectrometer  
274 (TES). The TES data agrees with what we found in the GMI-CTM model simulation,  
275 showing ozone enhancement over the tropical southeastern Pacific (150°W-60°W, 0-  
276 12°S) region in November 2006 relative to 2005 (~5-10 ppb at 250 hPa and 0-5 ppb at  
277 400 hPa, Figure 3 of Logan et al., 2008). The agreement between TES and GMI-CTM  
278 indicates a possible low bias of GMAO assimilated ozone during late 2006, as a result of  
279 the lack of emissions in the assimilation (Wargan et al., 2015).

280 Figure 4 shows the similar comparison as Figure 3, but over the two subtropical regions.  
281 Over the South Atlantic region, the assimilated ozone has similar but stronger IAV than  
282 that over the tropical southeastern Pacific region, showing the largest ozone year-by-year



283 variation ( $\sim 20$ ppb at 270 hPa) from October 2009 to October 2010, and the GMI-CTM  
284 simulation reproduces this variation quite well. Over the South Indian region, the  
285 assimilated ozone has weaker IAV than over other regions. Our model reproduces most  
286 of the variations in magnitude and phase, but shows anti-phase variations in late  
287 2006/early 2007, which substantially affected the calculated correlation coefficients  
288 between model and assimilated ozone. The simulated upper tropospheric ozone column  
289 reproduces well the IAV in the assimilated ozone column except for the late 2006. In  
290 general, agreement between the simulated and assimilated results confirms the suitability  
291 of the model for investigations of the controlling factors on the tropospheric ozone IAV  
292 over these regions.

293 The left column of Figure 5 presents the monthly profiles of correlation coefficients  
294 between the simulated ozone and StratO<sub>3</sub> over the four sub-regions. Strong positive  
295 correlations between StratO<sub>3</sub> and O<sub>3</sub> are observed in most seasons in the upper  
296 troposphere even over two tropical regions. Stratospheric influence plays a big role  
297 during austral winter-spring and reaches its seasonal maximum in August, when the  
298 subtropical jet system is strongest and moves to its northern-most location. Over the two  
299 subtropical regions, the strong stratospheric influence persists throughout the whole  
300 troposphere ( $r > 0.8$  at 700 hPa) in August. Over tropical south Atlantic region, the  
301 strong stratospheric influence is limited to the upper troposphere in austral winter-spring  
302 and decreases sharply with decreasing altitude. Over the tropical southeastern Pacific, the  
303 strong stratospheric influence persists year-long at the upper troposphere and reaches as  
304 low as  $\sim 400$  hPa except for December.

305 The right column of Figure 5 shows the seasonal profiles of correlation coefficients  
306 between ozone and ozone from emissions (emissO<sub>3</sub>). The emissO<sub>3</sub> is the difference  
307 between the simulations with varied and constant emission. Over the two subtropical  
308 regions, there are two seasonal maxima in the correlations between ozone and emissO<sub>3</sub>.  
309 The first occurs in September at the lower troposphere and decreases with increasing  
310 altitude, the second is in December/January showing opposite vertical gradient with  
311 stronger correlations in the upper and middle troposphere. Over the tropical southeastern  
312 Pacific region, the influence from emissions shows a similar double-peak pattern, but  
313 with the first maximum localized at the surface and the second peak localized in the



314 upper troposphere. Over the tropical south Atlantic, the influence of emissions is very  
315 small. South America and southern Africa are two major nearby burning regions.  
316 Emissions over South America have much larger IAV than those over southern Africa,  
317 although Africa emission is larger in absolute terms (Sauvage et al., 2007; Liu et al.,  
318 2010; Voulgarakis et al., 2015). Sauvage et al (2007) argued that emissions over the  
319 eastern regions (India, South-East Asia, Australia) could be transported southward in the  
320 upper troposphere through the Tropical Easterly Jet and affect ozone over Africa, the  
321 Atlantic and Indian Ocean (Hoskins and Rodwell, 1995; Rodwell and Hoskins, 2001).  
322 Meanwhile, emissions over the eastern region also show large IAV (Voulgarakis et al.,  
323 2015). Therefore, the interannual emission changes in South America (0-20°S, 72.5°W-  
324 37.5°W), southern Africa (5°S-20°S, 12°E-38°E) and the eastern region (70°E-125°E,  
325 10°S-40°N) may all affect the IAV of ozone due to emission changes in the southern  
326 hemisphere. In this study, we rely on tagged CO simulation to quantify the influence of  
327 biomass burning emissions from these three burning regions during months when  
328 emission IAV contributes significantly to the IAV of ozone.

329 In the next section, we choose August (the seasonal maximum of stratospheric input into  
330 the lower troposphere), September and December (the seasonal maximum of emission  
331 contribution) as three example months to examine the relative roles of different factors on  
332 IAV of tropospheric ozone over these regions.

### 333 **3.3 Factors controlling IAV in ozone in the middle and upper troposphere**

#### 334 **3.3.1 South Atlantic Region**

335 Figure 6 shows the multiple regression results over the South Atlantic region. It compares  
336 the simulated ozone anomalies to that calculated from two regression variables: StratO<sub>3</sub>  
337 and EmissO<sub>3</sub> at 270 hPa and 430 hPa in August, September and December. The fitted  
338 ozone anomalies in generally reproduce the IAV obtained from the GMI-CTM  
339 simulation. The explained proportion of variability in simulated ozone anomalies by  
340 StratO<sub>3</sub> and EmissO<sub>3</sub> is mostly above 50% and reaches as high as ~ 76% in December, at  
341 270 hPa, which demonstrates that StratO<sub>3</sub> and EmissO<sub>3</sub> are sufficient to explain the IAV  
342 of tropospheric ozone over the south Atlantic region. In August at 430 hPa, the fitted



343 ozone anomalies have a slightly weaker correlation with the simulated ozone and show  
344 less IAV compared to the ozone anomalies in GMI-CTM.

345 Figure 7 exhibits regression results in a way that highlights the relative contributions of  
346 the IAV of stratospheric input and emission on the IAV of ozone over South Atlantic.  
347 The three panels represent results from August, September and December from 1992 to  
348 2011. Each panel has two columns, which illustrate the respective contribution from  
349 changes in StratO<sub>3</sub> and EmissO<sub>3</sub> on the IAV of ozone mixing ratio. The left column of  
350 each panel compares the anomalies of StratO<sub>3</sub> (blue) and simulated ozone mixing ratio  
351 (black) from the GMI-CTM model at 270 and 430 hPa. The right column compares the  
352 simulated O<sub>3</sub> residual after removing the regression from StratO<sub>3</sub> (black line) and  
353 EmissO<sub>3</sub> (green line) at these two levels. The regression coefficient ( $\beta$ ) and its 95%  
354 confidence level are labeled in each panel and help us to determine whether the  
355 corresponding contribution is significant to explain the variation of simulated ozone. As  
356 discussed before, EmissO<sub>3</sub> reflects the effects from surface emission changes on ozone  
357 variations at interannual time scale. The stratospheric input reaches its seasonal  
358 maximum in August, during which the stratospheric contribution is significant  
359 throughout the troposphere, explaining about 70% of the simulated ozone variance at 270  
360 hPa and 41% at 430 hPa. The contributions from emission changes are very small and  
361 insignificant at these two levels in August. In September, the IAV of stratospheric input  
362 explains about 53% of the IAV in ozone at 270 hPa. The contribution decreases but is  
363 still significant at 430 hPa. The IAV of surface emissions contributes substantially to the  
364 IAV of ozone in September. The influence of emissions exceeds that of the stratosphere  
365 and explains about 50% of IAV in ozone at 430hPa. In December, the contributions from  
366 stratospheric input on the IAV of ozone are dominant (~60%) at 270 hPa but insignificant  
367 at 430 hPa. Emission influence is significant at both levels. However, unlike that of  
368 September, the influence of emissions on IAV of tropospheric ozone is great at 270 hPa  
369 (~40%) than at 430 hPa (~36%). We quantify emission contributions from three burning  
370 regions using a tagged CO simulation. Figure 8 shows standardized anomalies of the  
371 tagged CO tracers over South Atlantic from three burning source regions, including  
372 southern Africa (red), South America (blue) and eastern region (green) and their  
373 comparison with the EmissO<sub>3</sub> at 270 and 430 hPa in September and December from 1992



374 to 2011. The direct downwind transport of emissions from South America contributes  
375 most to the ozone variability from emissions over this region in September at both levels  
376 and the effects are most significant in the lower level (~58% at 430 hPa). In the upper  
377 troposphere, besides the contribution from S. America, the uplift and cross-equator  
378 transport of pollutants from eastern region also contributes (>10%) to the ozone variation  
379 over South Atlantic region. The contribution from southern Africa is small and less than  
380 10% at both levels. We also note that both StratO<sub>3</sub> and emissO<sub>3</sub> show a minimum in 2009  
381 and a maximum in 2010. There was a strong El Niño event in the year 2009/2010. Neu et  
382 al. (2014) identified the increased stratospheric circulation in 2010 driven by El  
383 Niño/easterly QBO based on TES data. A few other studies (e.g., Chen et al., 2011;  
384 Lewis et al., 2011) found that combined effects of 2009/2010 El Niño and warmer than  
385 normal Atlantic SST produced a severe drought over S. America and caused extensive  
386 biomass burning emission in 2010 dry season. Therefore, the agreements between  
387 changes in the StratO<sub>3</sub> and emissO<sub>3</sub> over 2009/2010 are at least partly driven by ENSO.  
388 Similar tropospheric ozone anomalies are observed after 1997 and 2006 El Niño event.  
389 Olsen et al. (2016) examined the magnitude and spatial distribution of ENSO effects on  
390 tropospheric column ozone using the assimilated fields and found a statistically  
391 significant negative response of tropospheric column ozone to ENSO over South Atlantic  
392 Ocean.

393 In December, emissions from South America and southern Africa do not contribute  
394 substantially to the IAV of emissO<sub>3</sub>. Emissions from eastern region dominate, explaining  
395 83% and 77% variance of emissO<sub>3</sub> IAV at 270 hPa and 430 hPa. The eastern pollutants  
396 have the strongest influence at the upper troposphere because of their transport pathway  
397 as discussed in Sauvage et al. (2007). Therefore, the emission contribution of  
398 tropospheric ozone IAV in December shows an opposite vertical structure to that seen in  
399 September.

400 In summary, over the South Atlantic region, the stratospheric input plays a dominant role  
401 in the upper troposphere with a seasonal maximum in August. At 430 hPa the  
402 contribution from emission changes to the IAV of ozone exceeds that of stratospheric  
403 input in September and December. A tagged CO simulation from 1992 to 2011 shows the  
404 direct downwind transport of pollutants from South America is the largest contributor to



405 emissO<sub>3</sub> in September, and it is strongest near the surface. In December, cross-equator  
406 transport of eastern region pollutants is the most important source of IAV due to  
407 emissions, and the effects are strongest in the upper troposphere.

### 408 **3.3.2 South Indian Ocean**

409 Over the south Indian Ocean, the fitted and simulated ozone anomalies are in excellent  
410 agreement (Figure 9). The explained proportion of variability in simulated ozone  
411 anomalies by StratO<sub>3</sub> and EmissO<sub>3</sub> is as high as ~ 88% in August at 270 hPa. We show  
412 relative contribution to the IAV in ozone due to stratospheric input and emission as  
413 obtained from multiple linear regression in Figure 10. In August and September,  
414 stratospheric input contributes more than 85% to ozone IAV at 270 hPa. The  
415 stratospheric contribution decreases slightly but is still dominant and significant at 430  
416 hPa (~50% in August and 64% in September). The emission contribution, which is  
417 mainly from downwind transport of pollutants from S. America and southern Africa  
418 (Figure 11), is most important at 430 hPa in September but accounts for only 27% of  
419 ozone IAV. The emission contribution is smaller in August. In December, both  
420 stratospheric input and surface emission influence the IAV of ozone. The contribution  
421 from stratospheric input slightly exceeds that from emissions at 270 hPa and becomes  
422 slightly weaker at 430 hPa. Examining the tagged sources simulation shows that emission  
423 from eastern regions is the largest sources of ozone IAV at 270 hPa and 430 hPa in  
424 December with a stronger influence at the upper troposphere (Figure 11).

425 These results show that stratospheric ozone makes a significant contribution to the  
426 tropospheric ozone variability over the South Indian Ocean, with the largest influence in  
427 the upper troposphere in austral winter. Emission influence from nearby pollution in the  
428 boundary layer is relatively weak and only significant in September, one month after the  
429 southern hemisphere peak-burning season. In the upper troposphere, the cross-equator  
430 transport of pollutants from the eastern region is the major emission source affecting the  
431 ozone variability. The influence peaks in December at the upper troposphere and extends  
432 to the middle troposphere.

### 433 **3.3.3 Tropical South Atlantic**



434 In the upper troposphere, lightning produces nitrogen oxides ( $\text{NO}_x$ ) and promotes the  
435 photochemical ozone production (e.g., Pickering et al., 1993). Murray et al. (2013) shows  
436 that the IAV of tropical tropospheric ozone column is sensitive to the IAV of lightning  
437 over the tropical south Atlantic region. We therefore add the lightning  $\text{NO}_x$  as the third  
438 variable besides  $\text{StratO}_3$  and  $\text{EmissO}_3$ . We test whether the addition of lightning  $\text{NO}_x$   
439 improves the regression model significantly. Figure 12 shows the comparison between  
440 simulated and fitted ozone anomalies without and with lightning  $\text{NO}_x$ . During the “dry  
441 season” months of August and September, when the subtropical jet related STE (Karoly  
442 et al., 1998; Bals-Elsholz et al., 2001; Nakamura and Shimpo, 2004) reaches a seasonal  
443 maximum, the lightning activities reach a seasonal minimum over the southern  
444 hemisphere. The fitted ozone anomalies based solely on  $\text{StratO}_3$  and  $\text{EmissO}_3$  (red) show  
445 high correlations ( $r = 0.8$  in August,  $r = 0.74$  in September) with that simulated from  
446 GMI-CTM at 270 hPa. Agreement between simulated and fitted ozone does not change in  
447 August and improves slightly in September by adding lightning  $\text{NO}_x$  in regression. In  
448 September, the simulated ozone anomaly shows a minimum ( $\sim -6$  ppb) in 2007 and a  
449 peak ( $\sim 5$  ppb) in 2010 at 430 hPa, but the IAV from 2007 to 2010 is almost missing in  
450 the fitted ozone anomaly, which indicates that other factors drive the IAV of ozone over  
451 tropical south Atlantic during this period. During the “wet season” month of December,  
452 the lightning activity reaches its seasonal maximum. Our regression based on  $\text{StratO}_3$  and  
453  $\text{EmissO}_3$  does not capture well the IAV of GMI-CTM simulated ozone at either level.  
454 The fitted ozone reproduces many of the IAV of simulated ozone after including  
455 lightning  $\text{NO}_x$  in the regression, indicating a strong influence from the lightning  $\text{NO}_x$  in  
456 December.

457 Figure 13 shows the regression results of relative contributions of stratospheric input and  
458 surface emission on the IAV of ozone. As discussed above, the tropical south Atlantic is  
459 in the descending branch of the Walker Circulation. Therefore, even though this region is  
460 located in the tropics, the IAV of stratospheric input still plays a dominant role and  
461 explains 64% in August and 50% in September of ozone variance in the upper  
462 troposphere. The stratospheric contribution, associated with radiative descent over this  
463 region, drops to less than 30% at 430 hPa but is still significant during these two months.  
464 Emission influences are not significant at either level in September. Examination of the



465 simulation shows that emission contribution is limited even at lower levels; the emission  
466 contribution becomes significant and explains ~30% variance of ozone at ~700 hPa (not  
467 shown). In December, neither stratospheric input nor emission contributes much to the  
468 IAV of ozone.

469 In the model, the lightning emissions take place in connection with deep convective  
470 events (Allen et al., 2010). Increase in deep convection produces more upper tropospheric  
471 NO<sub>x</sub> from lightning, which results in more ozone production. On the other hand, deep  
472 convection affects the upper tropospheric ozone budget through its direct transport of  
473 surface air. In December, biomass burning in the Southern Hemisphere is at its seasonal  
474 minimum. Air over tropical south Atlantic is relatively clean with low CO (Liu et al.,  
475 2010). Deep convection over a clean region reduces upper tropospheric ozone due to  
476 mixing. This effect could be positive if deep convection happens over a polluted region  
477 with relatively high ozone and its precursors (Lawrence et al., 2003). Use of the  
478 correlation to identify influence from the lightning NO<sub>x</sub> does not separate the two  
479 outcomes of IAV in convection, thus the sign of the correlation between variations in  
480 lightning NO<sub>x</sub> and upper tropospheric ozone can be positive or negative. The correlation  
481 is positive if the contribution from lightning NO<sub>x</sub> exceeds the contribution from  
482 convective transport or if transport of polluted air increases ozone. The correlation is  
483 negative if transport of clean air overwhelms ozone production from lightning NO<sub>x</sub>.  
484 Figure 14 compares the model residual after removing the contributions from StratO<sub>3</sub> and  
485 EmissO<sub>3</sub> with the lightning NO<sub>x</sub> at 270 hPa in September and December. In September  
486 the IAV of lightning plays a minor but significant role in the IAV of ozone in the upper  
487 troposphere. In December, the changes in lightning NO<sub>x</sub> have a significant impact on the  
488 ozone IAV, but show a negative correlation, which indicates that the transport and  
489 mixing of clean surface air exceeds ozone production from lightning NO<sub>x</sub> emissions with  
490 a net negative impact of IAV in convection.

### 491 3.3.4 Tropical southeastern Pacific

492 Figure 15, 16 and 17 show the similar comparisons but over the tropical southeastern  
493 Pacific region. The fitted ozone anomalies show moderate but still significant correlations  
494 with that simulated from GMI-CTM in August and September. In December, the fitted



495 ozone IAV agrees very well with the GMI-CTM simulated ozone IAV at 270 hPa. At 430  
496 hPa the agreement collapses and the fitted ozone does not show strong IAV as seen in the  
497 GMI-CTM simulated ozone (Figure 15). Figure 16 shows that IAV in stratospheric input  
498 significantly affects the ozone IAV during these three months, explaining 25-38% of the  
499 variance of simulated ozone at 270 hPa. Emissions contribution is quite small in August  
500 and September, but is significant and explains 28% of simulated ozone IAV in December  
501 at 270 hPa. The tagged CO simulations show that the tropical southeastern Pacific region  
502 is influenced by nearby pollutants from South America, and also by the cross-equator  
503 transport of pollutants from the eastern region (Figure 17). Previous studies (e.g.,  
504 Chandra et al., 1998; 2002; 2009; Sudo and Takahashi, 2001; Ziemke and Chandra, 2003;  
505 Doherty et al., 2006; Oman et al., 2011) show that ENSO has its strongest impact in the  
506 tropical Pacific basin. In August, the ITCZ is located at its northernmost location north of  
507 the Equator. Radiative sinking motion still dominates over the tropical southeastern  
508 Pacific in the middle - upper troposphere (Liu et al., 2010). Therefore, the emissions  
509 contribution from South America is quite small at 430 hPa and 270 hPa as shown in  
510 Figure 16. During an El Niño year, warmer SST with increase convection and large-scale  
511 upwelling start occurring in August, inhibiting the radiative sinking motion and resulting  
512 in ozone decrease in the middle-upper troposphere over this region. Our comparison  
513 shows strong negative correlation in August between IAV of middle-upper tropospheric  
514 ozone anomalies over this region and Niño 3.4 index during the past twenty years (Figure  
515 18).

#### 516 **4 Summary and Discussion**

517 Both model simulations and GEOS-5 assimilated ozone product derived from OMI/MLS  
518 show a tropospheric ozone column maximum centered over the south Atlantic from the  
519 equator to 30S. This ozone maximum extends westward to South America and the eastern  
520 equatorial Pacific; it extends southeastward to southern Africa and the south Indian  
521 Ocean. In this study, we use hindcast simulations from the GMI model of tropospheric  
522 and stratospheric chemistry, driven by assimilated MERRA meteorological fields, to  
523 interpret and quantify the relative importance of the stratospheric input and surface



524 emission to the interannual variations of tropospheric ozone over four sub-regions of the  
525 SHTOM from 1992 to 2011. Over the SHTOM region, IAV in the stratospheric  
526 contribution is found to be the most important factor driving the IAV of ozone, especially  
527 over the upper troposphere, where O<sub>3</sub> changes have strong radiative effects (Lacis et al.,  
528 1990). The IAV of the stratospheric contribution explains a large portion of variance in  
529 the tropospheric ozone especially during the austral winter season, even over two selected  
530 tropical regions. The strong influence of emission on ozone IAV is largely confined to  
531 the South Atlantic region in September.

532 Although the SHTOM looks like a continuous feature in the southern hemisphere, our  
533 study shows that the relative importance between stratospheric input and surface  
534 emissions changes over different subregions at different altitude. Over the two extra-  
535 tropics regions, the IAV of stratospheric contribution explains at least 50% of variance of  
536 the tropospheric ozone during its winter season. The IAV of ozone over the south Indian  
537 Ocean is dominantly driven by the IAV of stratospheric ozone contribution (>64%) with  
538 little or no influence from surface emissions at 270 hPa and 430 hPa. Over the south  
539 Atlantic region, besides the stratospheric ozone input, the IAV of surface emissions from  
540 South America and southern Africa also play a big role on the IAV of ozone, especially  
541 in the lower levels. The influence from emission exceeds that from the stratospheric  
542 contribution on the ozone variability in September at 430 hPa. In December, the emission  
543 influence mainly from remote transport of pollutants from eastern region is relatively  
544 high in the upper troposphere and decreases with the decreasing altitude.

545 Compared to the extra-tropics regions, the two tropical regions have a smaller influence  
546 from stratospheric input but the influence is still significant at both 270 hPa and 430 hPa  
547 in August and September. Over tropical south Atlantic region, the IAV of stratospheric  
548 input plays a dominant role and explains 64% in August and 52% in September of the  
549 ozone IAV at 270 hPa. The stratospheric contribution drops to less than half of that at  
550 270 hPa but is still significant at 430 hPa. Emission contributions are not significant at  
551 these two levels, even during September. Our model shows that the IAV of ozone is  
552 partially driven by the IAV of lightning in September. In December, the changes in  
553 lightning NO<sub>x</sub> have a significant impact on the ozone IAV, but show a negative  
554 correlation, which indicates that the transport and mixing of clean surface air exceeds



555 ozone production from lightning  $\text{NO}_x$  emissions with a net negative impact of IAV in  
556 convection. Over the tropical southeastern Pacific, IAV in stratospheric input  
557 significantly affects the ozone IAV during these three months, explaining 25-38% of the  
558 variance of simulated ozone at 270 hPa. Emissions have little or no influence in August,  
559 September at 270 hPa and 430 hPa, but are significant in December at 270 hPa,  
560 explaining 28% of simulated ozone IAV. A further comparison of ozone and ENSO  
561 index shows that ENSO, which affects the tropical convection and large-scale upwelling,  
562 shows a strong negative correlation with the IAV of tropospheric ozone over this region.  
563 Therefore, the model simulations/predictions with different convective parameterizations  
564 exhibit large uncertainties over this region as observed in Stevenson et al. (2006).  
565 In this study, our regional analysis based on the GMI-CTM model provides valuable  
566 conclusions on drivers of interannual variability over different subregions of the SHTOM  
567 and how they vary with the altitude. The quantification of their relative contributions on  
568 interannual time scales enhances our understanding of the IAV and, potentially, long-  
569 term trends in the tropospheric ozone and furthermore their effects to the radiative  
570 forcing change in climate.

### 571 **Acknowledgement**

572 All model output used for this article can be obtained by contacting J. Liu (email:  
573 junhua.liu@nasa.gov). I gratefully acknowledge the financial support by NASA's  
574 Atmospheric Chemistry Modeling and Analysis Program (ACMAP) (grants  
575 NNH12ZDA001N). Work was performed under contract with NASA at Goddard. I  
576 would like to thank K. Pickering, L. Oman, A. Thompson, H. Liu for their helpful  
577 discussion.

### 578 **References**

579 Allen, D., Pickering, K., Duncan, B., and Damon, M.: Impact of lightning NO emissions  
580 on North American photochemistry as determined using the Global Modeling Initiative  
581 (GMI) model, *Journal of Geophysical Research-Atmospheres*, 115, 2010.



- 582 Bals-Elsholz, T. M., Atallah, E. H., Bosart, L. F., Wasula, T. A., Cempa, M. J., and Lupo,  
583 A. R.: The wintertime Southern Hemisphere split jet: Structure, variability, and evolution,  
584 *Journal of Climate*, 14, 4191-4215, 2001.
- 585 Bjerknes, J.: Atmospheric teleconnections from the equatorial Pacific, *Mon. Weather*  
586 *Rev.*, 97(3), 163–172, 1969.
- 587 Chandra, S., Ziemke, J. R., Bhartia, P. K., and Martin, R. V.: Tropical tropospheric  
588 ozone: Implications for dynamics and biomass burning, *Journal of Geophysical*  
589 *Research-Atmospheres*, 107, 2002.
- 590 Chandra, S., Ziemke, J. R., Duncan, B. N., Diehl, T. L., Livesey, N. J., and Froidevaux,  
591 L.: Effects of the 2006 El Niño on tropospheric ozone and carbon monoxide: implications  
592 for dynamics and biomass burning, *Atmospheric Chemistry and Physics*, 9, 4239-4249,  
593 2009.
- 594 Chandra, S., Ziemke, J. R., Min, W., and Read, W. G.: Effects of 1997-1998 El Niño on  
595 tropospheric ozone and water vapor, *Geophysical Research Letters*, 25, 3867-3870, 1998.
- 596 Chen, Y., Randerson, J. T., Morton, D. C., DeFries, R. S., Collatz, G. J., Kasibhatla, P.  
597 S., Giglio, L., Jin, Y., and Marlier, M. E.: Forecasting Fire Season Severity in South  
598 America Using Sea Surface Temperature Anomalies, *Science*, 334, 787-791, 2011.
- 599 Chin, M., Ginoux, P., Kinne, S., Torres, O., Holben, B. N., Duncan, B. N., Martin, R. V.,  
600 Logan, J. A., Higurashi, A., and Nakajima, T.: Tropospheric aerosol optical thickness  
601 from the GOCART model and comparisons with satellite and Sun photometer  
602 measurements, *J ATMOS SCI*, 59, 461-483, 2002.
- 603 Danielsen, E. F., Stratospheric-Tropospheric Exchange Based on Radioactivity, Ozone  
604 and Potential Vorticity, *Journal of the Atmospheric Sciences*, 25, 502-518, 1968.
- 605 Doherty, R. M., Stevenson, D. S., Johnson, C. E., Collins, W. J., and Sanderson, M. G.:  
606 Tropospheric ozone and El Niño-Southern Oscillation: Influence of atmospheric  
607 dynamics, biomass burning emissions, and future climate change, *Journal of Geophysical*  
608 *Research-Atmospheres*, 111, 2006.
- 609 Duncan, B. N., Strahan, S. E., Yoshida, Y., Steenrod, S. D., and Livesey, N.: Model study  
610 of the cross-tropopause transport of biomass burning pollution, *ATMOS CHEM PHYS*,  
611 7, 3713-3736, 2007.



- 612 Eyring, V., Lamarque, J.-F., Hess, P., Arfeuille, F., Bowman, K., Chipperfield, M. P.,  
613 Duncan, B., Fiore, A., Gettelman, A., Giorgetta, M. A., Granier, C., Kinnison, M. H. D.,  
614 Kunze, M., Langematz, U., Luo, B., Martin, R., Matthes, K., Newman, P. A., Peter, T.,  
615 Robock, A., Ryerson, T., Saiz-Lopez, A., Salawitch, R., Schultz, M., Shepherd, T. G.,  
616 Shindell, D., Staehelin, J., Tegtmeier, S., Thomason, L., Tilmes, S., Vernier, J.-P.,  
617 Waugh, D. W., and Young, P. J.: Overview of IGAC/SPARC Chemistry-Climate  
618 Model Initiative (CCMI) Community Simulations in Support of Upcoming Ozone  
619 and Climate Assessments. In: SPARC Newsletter 40, 48, WMO/SPARC, Zürich, 2013.
- 620 Fishman, J., Watson, C. E., Larsen, J. C., and Logan, J. A.: DISTRIBUTION OF  
621 TROPOSPHERIC OZONE DETERMINED FROM SATELLITE DATA, Journal of  
622 Geophysical Research-Atmospheres, 95, 3599-3617, 1990.
- 623 Folkens, I., Braun, C., Thompson, A. M., and Witte, J.: Tropical ozone as an indicator of  
624 deep convection, Journal of Geophysical Research-Atmospheres, 107, 2002.
- 625 Hoskins, B. J. and Rodwell, M. J.: A MODEL OF THE ASIAN SUMMER MONSOON  
626 .1. THE GLOBAL-SCALE, Journal of the Atmospheric Sciences, 52, 1329-1340, 1995.
- 627 Jacob, D. J., Heikes, B. G., Fan, S. M., Logan, J. A., Mauzerall, D. L., Bradshaw, J. D.,  
628 Singh, H. B., Gregory, G. L., Talbot, R. W., Blake, D. R., and Sachse, G. W.: Origin of  
629 ozone and NO<sub>x</sub> in the tropical troposphere: A photochemical analysis of aircraft  
630 observations over the South Atlantic basin, Journal of Geophysical Research-  
631 Atmospheres, 101, 24235-24250, 1996.
- 632 Jenkins, G. S. and Ryu, J. H.: Linking horizontal and vertical transports of biomass fire  
633 emissions to the tropical Atlantic ozone paradox during the Northern Hemisphere winter  
634 season: climatology, Atmospheric Chemistry and Physics, 4, 449-469, 2004a.
- 635 Jenkins, G. S. and Ryu, J. H.: Space-borne observations link the tropical Atlantic ozone  
636 maximum and paradox to lightning, Atmospheric Chemistry and Physics, 4, 361-375,  
637 2004b.
- 638 Jourdain, L., Worden, H. M., Worden, J. R., Bowman, K., Li, Q., Eldering, A., Kulawik,  
639 S. S., Osterman, G., Boersma, K. F., Fisher, B., Rinsland, C. P., Beer, R., and Gunson,  
640 M.: Tropospheric vertical distribution of tropical Atlantic ozone observed by TES during  
641 the northern African biomass burning season, Geophysical Research Letters, 34, 2007.



- 642 Julian, P. R. and Chervin, R. M.: A study of the Southern Oscillation and Walker  
643 Circulation phenomenon, *Mon. Weather Rev.*, 106(10), 1433–1451, 1978.
- 644 Karoly, D. J., Vincent, D. G., and Schrage, J. M.: Meteorology of the Southern  
645 Hemisphere, American Meteorological Society, 45 Beacon St., Boston, MA, 02108,  
646 1998.
- 647 Kim, P. S., Jacob, D. J., Liu, X., Warner, J. X., Yang, K., Chance, K., Thouret, V., and  
648 Nedelec, P.: Global ozone-CO correlations from OMI and AIRS: constraints on  
649 tropospheric ozone sources, *Atmospheric Chemistry and Physics*, 13, 9321-9335, 2013.
- 650 Lacis, A. A., Wuebbles, D. J., and Logan, J. A.: RADIATIVE FORCING OF CLIMATE  
651 BY CHANGES IN THE VERTICAL-DISTRIBUTION OF OZONE, *Journal of*  
652 *Geophysical Research-Atmospheres*, 95, 9971-9981, 1990.
- 653 Lawrence, M. G., von Kuhlmann, R., Salzmann, M., and Rasch, P. J.: The balance of  
654 effects of deep convective mixing on tropospheric ozone, *Geophysical Research Letters*,  
655 30, 2003.
- 656 Lewis, S. L., Brando, P. M., Phillips, O. L., van der Heijden, G. M. F., and Nepstad, D.:  
657 The 2010 Amazon Drought, *Science*, 331, 554-554, 2011.
- 658 Lin, M., Fiore, A. M., Cooper, O. R., Horowitz, L. W., Langford, A. O., Levy II, H.,  
659 Johnson, B. J., Vaishali Naik, V., Oltmans, S. J., and Senff, C. J.: Springtime high surface  
660 ozone events over the western United States: Quantifying the role of stratospheric  
661 intrusions, Submitted to *JGR-Atmosphere*, CalNex Special Section, 2012.
- 662 Liu, J., Logan, J. A., Jones, D. B. A., Livesey, N. J., Megretskaia, I., Carouge, C., and  
663 Nedelec, P.: Analysis of CO in the tropical troposphere using Aura satellite data and the  
664 GEOS-Chem model: insights into transport characteristics of the GEOS meteorological  
665 products, *Atmospheric Chemistry and Physics*, 10, 12207-12232, 2010.
- 666 Liu, J., Logan, J. A., Murray, L. T., Pumphrey, H. C., Schwartz, M. J., and Megretskaia,  
667 I. A.: Transport analysis and source attribution of seasonal and interannual variability of  
668 CO in the tropical upper troposphere and lower stratosphere, *Atmospheric Chemistry and*  
669 *Physics*, 13, 129-146, 2013.
- 670 Liu, J., Rodriguez, J. M., Thompson, A. M., Logan, J. A., Douglass, A. R., Olsen, M. A.,  
671 Steenrod, S. D., and Posny, F.: Origins of tropospheric ozone interannual variation over



- 672 Reunion: A model investigation, *Journal of Geophysical Research-Atmospheres*, 121,  
673 521-537, 2016.
- 674 Logan, J. A., Megretskaia, I., Nassar, R., Murray, L. T., Zhang, L., Bowman, K. W.,  
675 Worden, H. M., and Luo, M.: Effects of the 2006 El Niño on tropospheric composition as  
676 revealed by data from the Tropospheric Emission Spectrometer (TES), *Geophysical*  
677 *Research Letters*, 35, 2008.
- 678 Logan, J. A., Prather, M. J., Wofsy, S. C., and McElroy, M. B.: TROPOSPHERIC  
679 CHEMISTRY - A GLOBAL PERSPECTIVE, *Journal of Geophysical Research-Oceans*  
680 *and Atmospheres*, 86, 7210-7254, 1981.
- 681 Martin, R. V., Jacob, D. J., Logan, J. A., Bey, I., Yantosca, R. M., Staudt, A. C., Li, Q.  
682 B., Fiore, A. M., Duncan, B. N., Liu, H. Y., Ginoux, P., and Thouret, V.: Interpretation of  
683 TOMS observations of tropical tropospheric ozone with a global model and in situ  
684 observations, *Journal of Geophysical Research-Atmospheres*, 107, 2002.
- 685 Murray, L. T., Logan, J. A., and Jacob, D. J.: Interannual variability in tropical  
686 tropospheric ozone and OH: The role of lightning, *Journal of Geophysical Research-*  
687 *Atmospheres*, 118, 11468-11480, 2013.
- 688 Nakamura, H. and Shimpo, A.: Seasonal Variations in the Southern Hemisphere Storm  
689 Tracks and Jet Streams as Revealed in a Reanalysis Dataset., *J. Climate*, 17, 1828–1844.,  
690 2004.
- 691 Neu, J. L., Flury, T., Manney, G. L., Santee, M. L., Livesey, N. J., and Worden, J.:  
692 Tropospheric ozone variations governed by changes in stratospheric circulation, *Nature*  
693 *Geoscience*, 7, 340-344, 2014.
- 694 Olsen, M. A., Wargan, K., and Pawson, S.: Tropospheric column ozone response to  
695 ENSO in GEOS-5 assimilation of OMI and MLS ozone data, *Atmospheric Chemistry*  
696 *and Physics*, 16, 7091-7103, 2016.
- 697 Oman, L. D., Douglass, A. R., Ziemke, J. R., Rodriguez, J. M., Waugh, D. W., and  
698 Nielsen, J. E.: The ozone response to ENSO in Aura satellite measurements and a  
699 chemistry-climate simulation, *Journal of Geophysical Research-Atmospheres*, 118, 965-  
700 976, 2013.



- 701 Oman, L. D., Ziemke, J. R., Douglass, A. R., Waugh, D. W., Lang, C., Rodriguez, J. M.,  
702 and Nielsen, J. E.: The response of tropical tropospheric ozone to ENSO, Geophysical  
703 Research Letters, 38, 2011.
- 704 Pickering, K. E., Thompson, A. M., Tao, W. K., and Kucsera, T. L.: UPPER  
705 TROPOSPHERIC OZONE PRODUCTION FOLLOWING MESOSCALE  
706 CONVECTION DURING STEP EMEX, Journal of Geophysical Research-Atmospheres,  
707 98, 8737-8749, 1993.
- 708 Pickering, K. E., Thompson, A. M., Wang, Y. S., Tao, W. K., McNamara, D. P.,  
709 Kirchhoff, V., Heikes, B. G., Sachse, G. W., Bradshaw, J. D., Gregory, G. L., and Blake,  
710 D. R.: Convective transport of biomass burning emissions over Brazil during TRACE A,  
711 Journal of Geophysical Research-Atmospheres, 101, 23993-24012, 1996.
- 712 Prather, M. J., Zhu, X., Tang, Q., Hsu, J. N., and Neu, J. L.: An atmospheric chemist in  
713 search of the tropopause, J GEOPHYS RES-ATMOS, 116, D04306, 2011.
- 714 Rienecker, M. M., Suarez, M. J., Gelaro, R., Todling, R., Bacmeister, J., Liu, E.,  
715 Bosilovich, M. G., Schubert, S. D., Takacs, L., Kim, G.-K., Bloom, S., Chen, J., Collins,  
716 D., Conaty, A., Da Silva, A., Gu, W., Joiner, J., Koster, R. D., Lucchesi, R., Molod, A.,  
717 Owens, T., Pawson, S., Pegion, P., Redder, C. R., Reichle, R., Robertson, F. R., Ruddick,  
718 A. G., Sienkiewicz, M., and Woollen, J.: MERRA: NASA's Modern-Era Retrospective  
719 Analysis for Research and Applications, Journal of Climate, 24, 3624-3648, 2011.
- 720 Rodwell, M. J. and Hoskins, B. J.: Subtropical anticyclones and summer monsoons,  
721 Journal of Climate, 14, 3192-3211, 2001.
- 722 Sauvage, B., Martin, R. V., van Donkelaar, A., and Ziemke, J. R.: Quantification of the  
723 factors controlling tropical tropospheric ozone and the South Atlantic maximum, Journal  
724 of Geophysical Research-Atmospheres, 112, 2007.
- 725 Sauvage, B., Thouret, V., Thompson, A. M., Witte, J. C., Cammas, J. P., Nedelec, P., and  
726 Athier, G.: Enhanced view of the "tropical Atlantic ozone paradox" and "zonal wave one"  
727 from the in situ MOZAIC and SHADOZ data, Journal of Geophysical Research-  
728 Atmospheres, 111, 2006.
- 729 Solomon, S., Thompson, D. W. J., Portmann, R. W., Oltmans, S. J., and Thompson, A.  
730 M.: On the distribution and variability of ozone in the tropical upper troposphere:



- 731 Implications for tropical deep convection and chemical-dynamical coupling, *Geophysical*  
732 *Research Letters*, 32, 2005.
- 733 Stevenson, D. S., Dentener, F. J., Schultz, M. G., Ellingsen, K., van Noije, T. P. C., Wild,  
734 O., Zeng, G., Amann, M., Atherton, C. S., Bell, N., Bergmann, D. J., Bey, I., Butler, T.,  
735 Cofala, J., Collins, W. J., Derwent, R. G., Doherty, R. M., Drevet, J., Eskes, H. J., Fiore,  
736 A. M., Gauss, M., Hauglustaine, D. A., Horowitz, L. W., Isaksen, I. S. A., Krol, M. C.,  
737 Lamarque, J. F., Lawrence, M. G., Montanaro, V., Muller, J. F., Pitari, G., Prather, M. J.,  
738 Pyle, J. A., Rast, S., Rodriguez, J. M., Sanderson, M. G., Savage, N. H., Shindell, D. T.,  
739 Strahan, S. E., Sudo, K., and Szopa, S.: Multimodel ensemble simulations of present-day  
740 and near-future tropospheric ozone, *Journal of Geophysical Research-Atmospheres*, 111,  
741 2006.
- 742 Stohl, A., Bonasoni, P., Cristofanelli, P., Collins, W., Feichter, J., Frank, A., Forster, C.,  
743 Gerasopoulos, E., Gaggeler, H., James, P., Kentarchos, T., Kromp-Kolb, H., Kruger, B.,  
744 Land, C., Meloan, J., Papayannis, A., Priller, A., Seibert, P., Sprenger, M., Roelofs, G. J.,  
745 Scheel, H. E., Schnabel, C., Siegmund, P., Tobler, L., Trickl, T., Wernli, H., Wirth, V.,  
746 Zanis, P., and Zerefos, C.: Stratosphere-troposphere exchange: A review, and what we  
747 have learned from STACCATO, *Journal of Geophysical Research-Atmospheres*, 108,  
748 2003.
- 749 Strahan, S. E., Douglass, A. R., and Newman, P. A.: The contributions of chemistry and  
750 transport to low arctic ozone in March 2011 derived from Aura MLS observations,  
751 *Journal of Geophysical Research-Atmospheres*, 118, 1563-1576, 2013.
- 752 Strahan, S. E., Duncan, B. N., and Hoor, P.: Observationally derived transport diagnostics  
753 for the lowermost stratosphere and their application to the GMI chemistry and transport  
754 model, *ATMOS CHEM PHYS*, 7, 2435-2445, 2007.
- 755 Strode, S. A., Rodriguez, J. M., Logan, J. A., Cooper, O. R., Witte, J. C., Lamsal, L. N.,  
756 Damon, M., Van Aartsen, B., Steenrod, S. D., and Strahan, S. E.: Trends and variability  
757 in surface ozone over the United States, *Journal of Geophysical Research-Atmospheres*,  
758 120, 9020-9042, 2015.
- 759 Sudo, K. and Takahashi, M.: Simulation of tropospheric ozone changes during 1997-  
760 1998 El Niño: Meteorological impact on tropospheric photochemistry, *Geophysical*  
761 *Research Letters*, 28, 4091-4094, 2001.



- 762 Thompson, A. M., Pickering, K. E., McNamara, D. P., Schoeberl, M. R., Hudson, R. D.,  
763 Kim, J. H., Browell, E. V., Kirchhoff, V., and Nganga, D.: Where did tropospheric ozone  
764 over southern Africa and the tropical Atlantic come from in October 1992? Insights from  
765 TOMS, GTE TRACE A, and SAFARI 1992, *Journal of Geophysical Research-*  
766 *Atmospheres*, 101, 24251-24278, 1996.
- 767 Thompson, A. M., Witte, J. C., McPeters, R. D., Oltmans, S. J., Schmidlin, F. J., Logan,  
768 J. A., Fujiwara, M., Kirchhoff, V., Posny, F., Coetzee, G. J. R., Hoegger, B., Kawakami,  
769 S., Ogawa, T., Johnson, B. J., Vomel, H., and Labow, G.: Southern Hemisphere  
770 Additional Ozonesondes (SHADOZ) 1998-2000 tropical ozone climatology - 1.  
771 Comparison with Total Ozone Mapping Spectrometer (TOMS) and ground-based  
772 measurements, *Journal of Geophysical Research-Atmospheres*, 108, 2003.
- 773 Thouret, V., Saunois, M., Minga, A., Mariscal, A., Sauvage, B., Solete, A., Agbangla, D.,  
774 Nedelec, P., Mari, C., Reeves, C. E., and Schlager, H.: An overview of two years of  
775 ozone radio soundings over Cotonou as part of AMMA, *Atmospheric Chemistry and*  
776 *Physics*, 9, 6157-6174, 2009.
- 777 Tocquer, F., Barret, B., Mari, C., Le Flochmoen, E., Cammas, J. P., and Sauvage, B.: An  
778 upper tropospheric 'ozone river' from Africa to India during the 2008 Asian post-  
779 monsoon season, *Tellus Series B-Chemical and Physical Meteorology*, 67, 2015.
- 780 Voulgarakis, A., Marlier, M. E., Faluvegi, G., Shindell, D. T., Tsigaridis, K., and  
781 Mangeon, S.: Interannual variability of tropospheric trace gases and aerosols: The role of  
782 biomass burning emissions, *Journal of Geophysical Research-Atmospheres*, 120, 7157-  
783 7173, 2015.
- 784 Voulgarakis, A., Savage, N. H., Wild, O., Braesicke, P., Young, P. J., Carver, G. D., and  
785 Pyle, J. A.: Interannual variability of tropospheric composition: the influence of changes  
786 in emissions, meteorology and clouds, *Atmospheric Chemistry and Physics*, 10, 2491-  
787 2506, 2010.
- 788 Wargan, K., Pawson, S., Olsen, M. A., Witte, J. C., Douglass, A. R., Ziemke, J. R.,  
789 Strahan, S. E., and Nielsen, J. E.: The global structure of upper troposphere-lower  
790 stratosphere ozone in GEOS-5: A multiyear assimilation of EOS Aura data, *Journal of*  
791 *Geophysical Research-Atmospheres*, 120, 2013-2036, 2015.



792 Weller, R., Lilischkis, R., Schrems, O., Neuber, R., and Wessel, S.: Vertical ozone  
793 distribution in the marine atmosphere over the central Atlantic Ocean (56 degrees S 50  
794 degrees N), *Journal of Geophysical Research-Atmospheres*, 101, 1387-1399, 1996.

795 WMO: Scientific Assessment of Ozone Depletion: 2014, Global Ozone Research and  
796 Monitoring Project, World Meteorological Organization, Geneva, Switzerland, 2014.

797 Zeng, G. and Pyle, J. A.: Influence of El Niño Southern Oscillation on  
798 stratosphere/troposphere exchange and the global tropospheric ozone budget,  
799 *Geophysical Research Letters*, 32, 2005.

800 Ziemke, J. R. and Chandra, S.: La Nina and El Niño-induced variabilities of ozone in the  
801 tropical lower atmosphere during 1970-2001, *Geophysical Research Letters*, 30, 2003.

802 Ziemke, J. R., Chandra, S., Oman, L. D., and Bhartia, P. K.: A new ENSO index derived  
803 from satellite measurements of column ozone, *Atmospheric Chemistry and Physics*, 10,  
804 3711-3721, 2010.

805 Ziemke, J. R., Chandra, S., Thompson, A. M., and McNamara, D. P.: Zonal asymmetries  
806 in southern hemisphere column ozone: Implications of biomass burning, *Journal of*  
807 *Geophysical Research-Atmospheres*, 101, 14421-14427, 1996.

808 Ziemke, J. R., Olsen, M. A., Witte, J. C., Douglass, A. R., Strahan, S. E., Wargan, K.,  
809 Liu, X., Schoeberl, M. R., Yang, K., Kaplan, T. B., Pawson, S., Duncan, B. N., Newman,  
810 P. A., Bhartia, P. K., and Heney, M. K.: Assessment and applications of NASA ozone  
811 data products derived from Aura OMI/MLS satellite measurements in context of the GMI  
812 chemical transport model, *Journal of Geophysical Research-Atmospheres*, 119, 5671-  
813 5699, 2014.

814

815

816

817

818

819

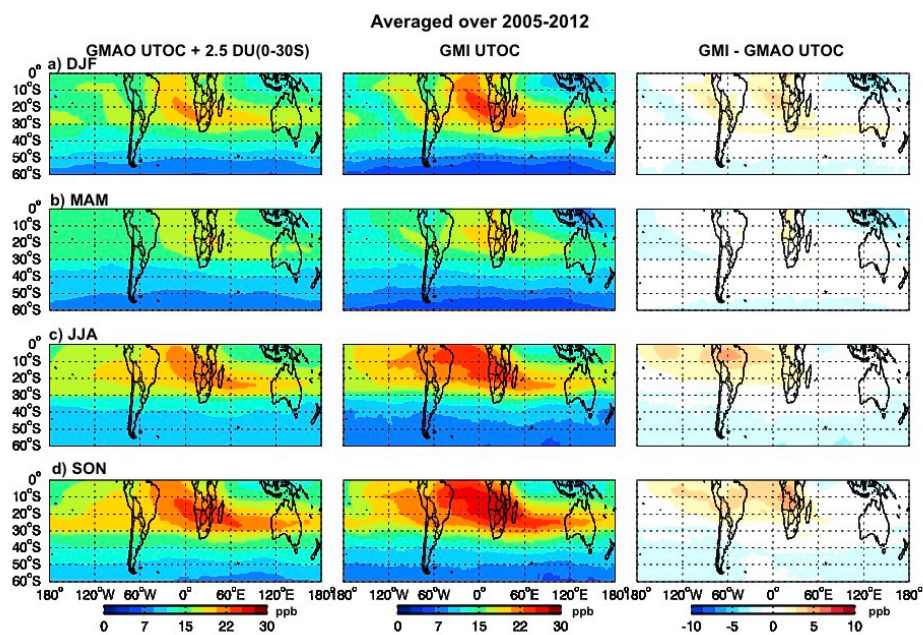
820

821

822

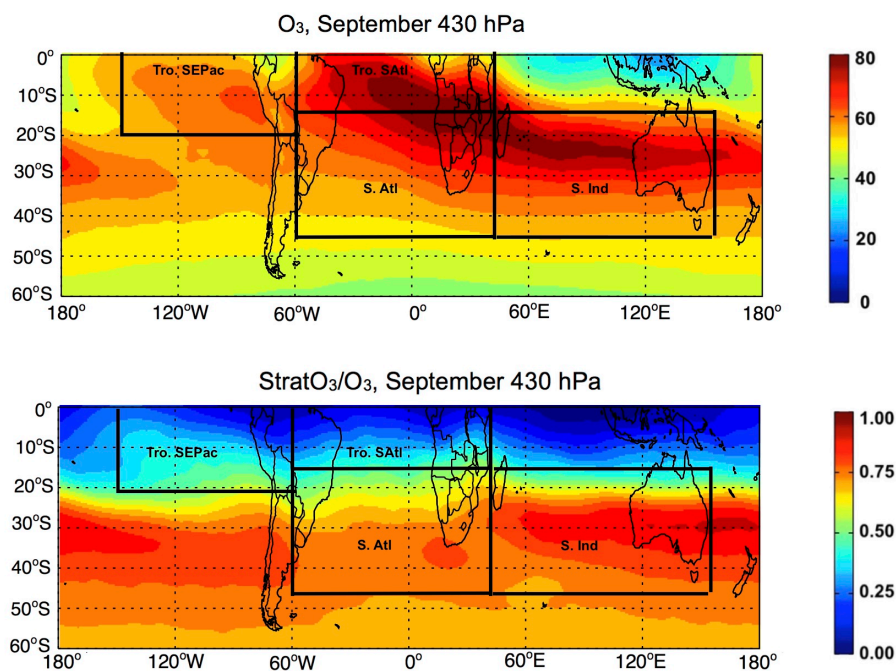


823 **Figures:**



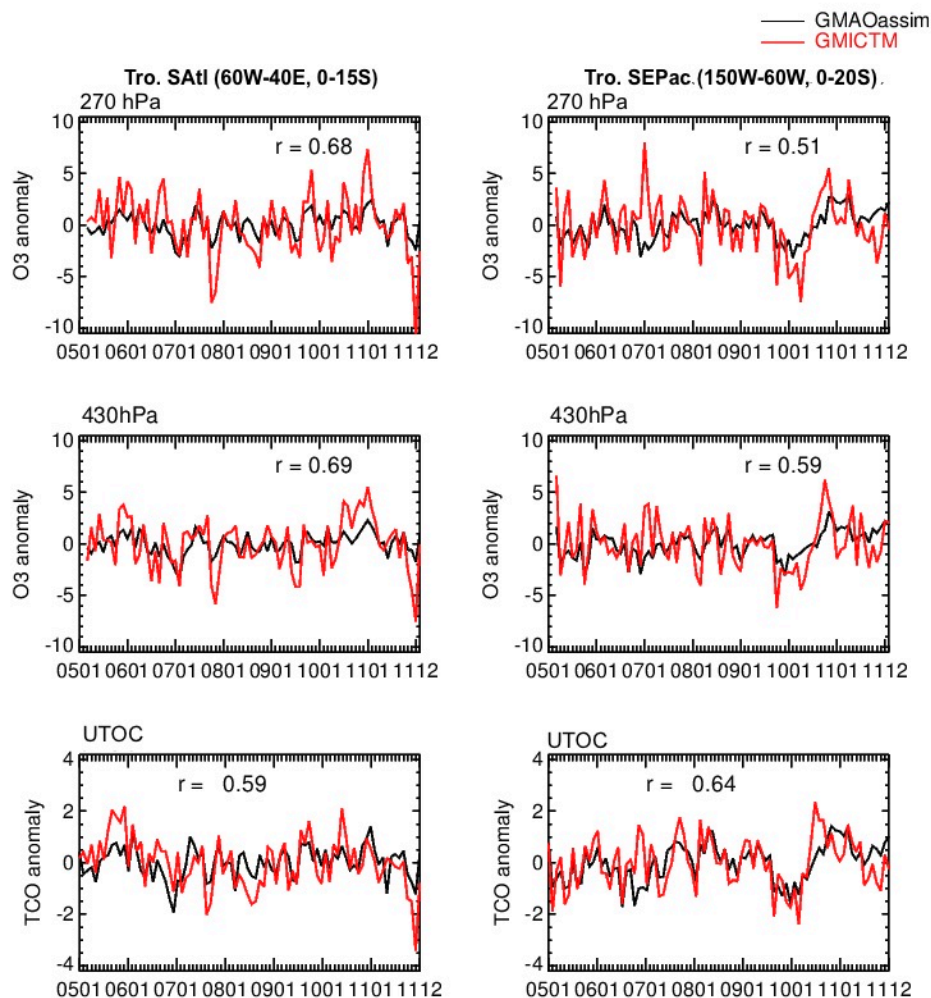
824

825 **Figure 1:** Seasonal climatology of upper tropospheric column ozone (UTOC) (in Dobson Units) for (a)  
826 December-January-February (DJF), (b) March-April-May (MAM), (c) June-July-August (JJA), and (d)  
827 September-October-November (SON) averaged from 2005 to 2012 for GMAO assimilated ozone (left) and GMI-  
828 CTM Hindcast-VE ozone (middle) and their absolute difference (right). The GMAO assimilated ozone has been  
829 adjusted by adding 2.5 DU in 0-30° S based on Wargan et al. (2015).



830

831 **Figure 2:** The simulated ozone (top) and the  $\text{StratO}_3/\text{O}_3$  (bottom) at 430 hPa averaged over 1991-2011 in  
832 **September.** Stronger stratospheric influence happens over southern hemisphere centered on 30° S, co-locating  
833 with subtropical jet stream regions with descending stratospheric air. The black boxes show four regions  
834 discussed in this study. From left to right: (1) Tropical southeastern Pacific (0-20° S, 150° W-60° W); (2)  
835 Tropical South Atlantic region (0-15° S, 60° W-40° E); (3) Subtropical South Atlantic region (15° S-45° S, 60° W-  
836 40° E); (4) Subtropical South Indian Ocean (15° S-45° S, 40° E-150° E).



837

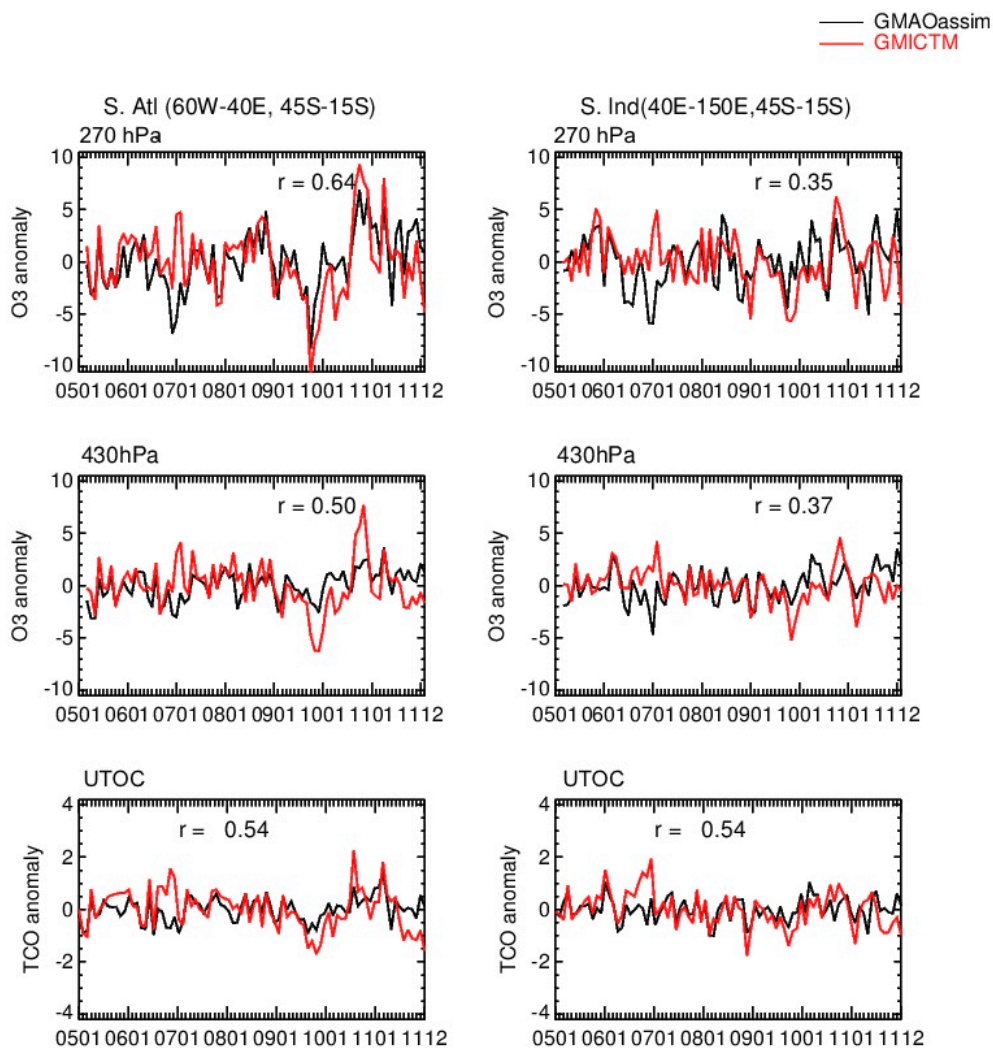
838

839

840

841

Figure 3: Time series plots of tropospheric ozone anomalies (unit: ppb) from GMAO assimilated data (black) and GMI-CTM (red) at 270 hPa and 430 hPa and upper tropospheric ozone column (UTOC, integrated from 500 hPa to the tropopause) anomalies over (left) Tropical South Atlantic region (0-15° S, 60° W-40° E); (right) Tropical southeastern Pacific (0-20° S, 150° W-60° W) from 2005 to 2011.



842

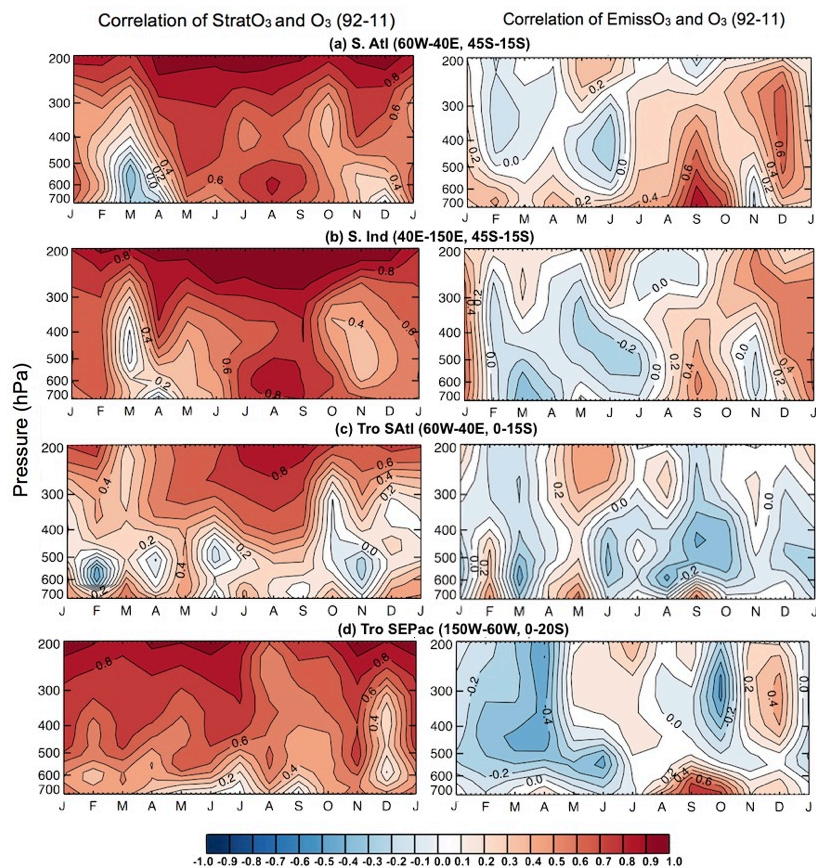
843

844

845

846

**Figure 4:** Time series plots of tropospheric ozone anomalies (unit: ppb) from GMAO assimilated data (black) and GMI-CTM (red) at 270 hPa and 430 hPa and upper tropospheric ozone column (UTOC, integrated from 500 hPa to the tropopause) anomalies over (left) South Atlantic (15° S-45° S, 60° W-40° E); (right) South Indian Ocean (15° S-45° S, 40° E-150° E) from 2005 to 2011.



847

848

Figure 5: Monthly profile maps of correlations coefficients between ozone and left) StratO<sub>3</sub>, right) EmissO<sub>3</sub>

849

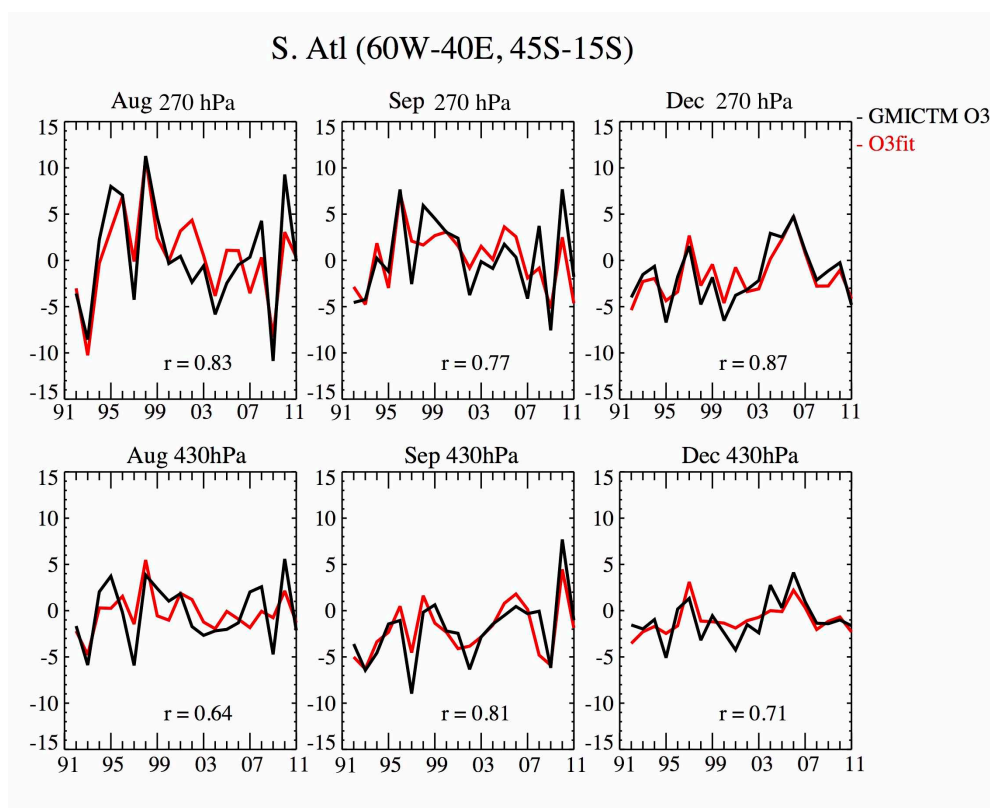
from 1992 to 2011 over (a) South Atlantic (15° S-45° S, 60° W-40° E); (b) South Indian Ocean (15° S-45° S, 40°

850

E-150° E); (c) Tropical South Atlantic region (0-15° S, 60° W-40° E); (d) Tropical southeastern Pacific (0-20° S,

851

150° W-60° W). Y-axis is pressure in unit hPa.



852

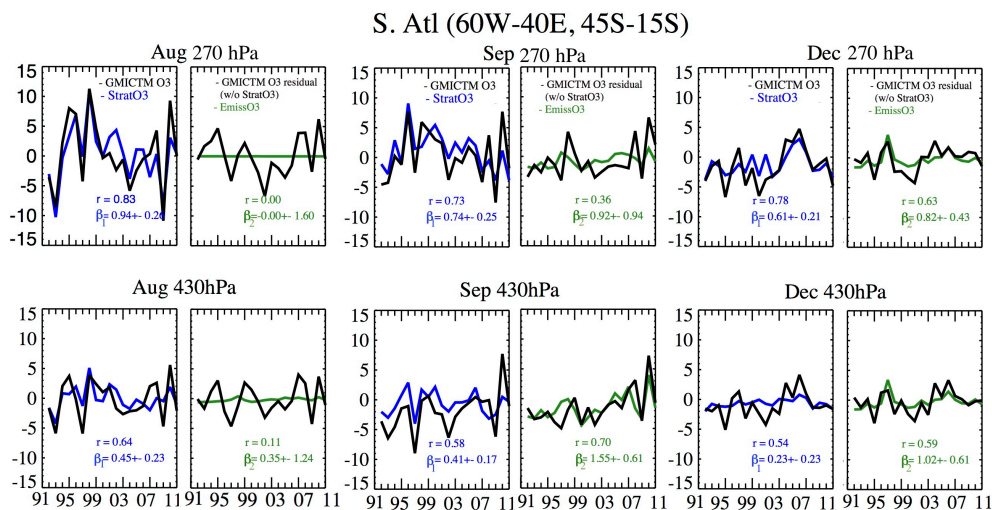
853 **Figure 6: Comparison of the simulated ozone anomalies and the calculated ozone anomalies relying on two**

854 **predictor variables: StratO<sub>3</sub>, EmissO<sub>3</sub> at 270 hPa and 430 hPa over South Atlantic region. Three panels show**

855 **results from August (left), September (middle) and December (right) from 1992 to 2011. Unit for y-axis is ppb.**

856

857



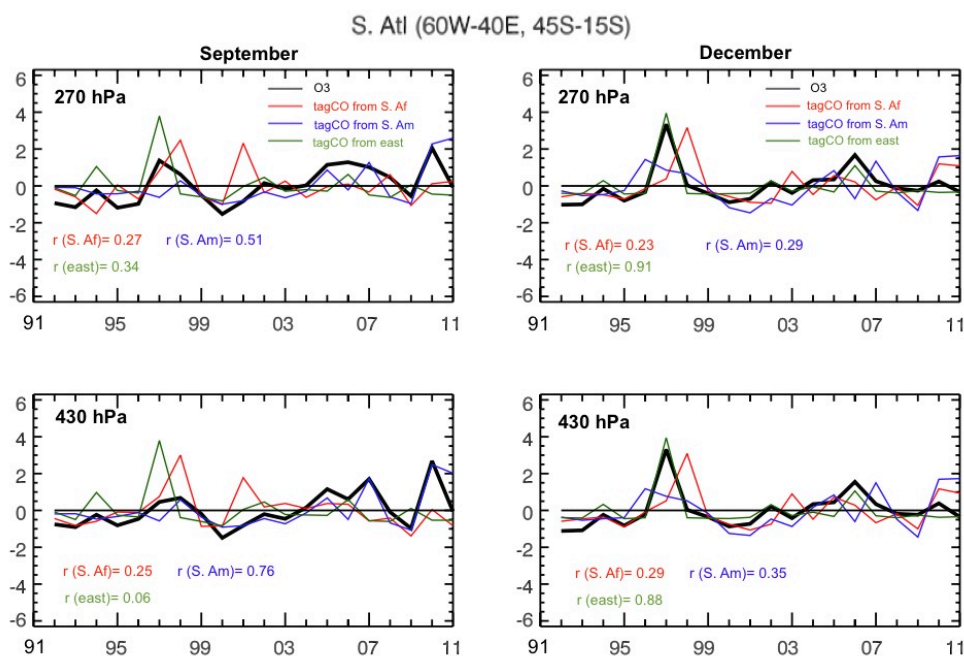
858

859

860 **Figure 7: The multi-regression results of simulated ozone anomalies over South Atlantic region relying on two**  
 861 **predictor variables: StratO<sub>3</sub> (blue), EmissO<sub>3</sub> (green) at 270 hPa and 430 hPa. Three panels show results from**  
 862 **August (left), September (middle) and December (right) from 1992 to 2011. Each panel contains two columns.**  
 863 **The left column of each panel compares the anomalies of StratO<sub>3</sub> (blue) and simulated ozone mixing ratio**  
 864 **(black) from the GMI-CTM model at 270 and 430 hPa. The right column compares the simulated O<sub>3</sub> residual**  
 865 **after removing the regression from StratO<sub>3</sub> (black line) and EmissO<sub>3</sub> (green line) at these two levels. EmissO<sub>3</sub> is**  
 866 **calculated from the difference of simulated ozone between the run with yearly-varied emission and the run with**  
 867 **constant emission. Unit for y-axis is ppb. The correlation (r), regression coefficient (β) and its 95% confidence**



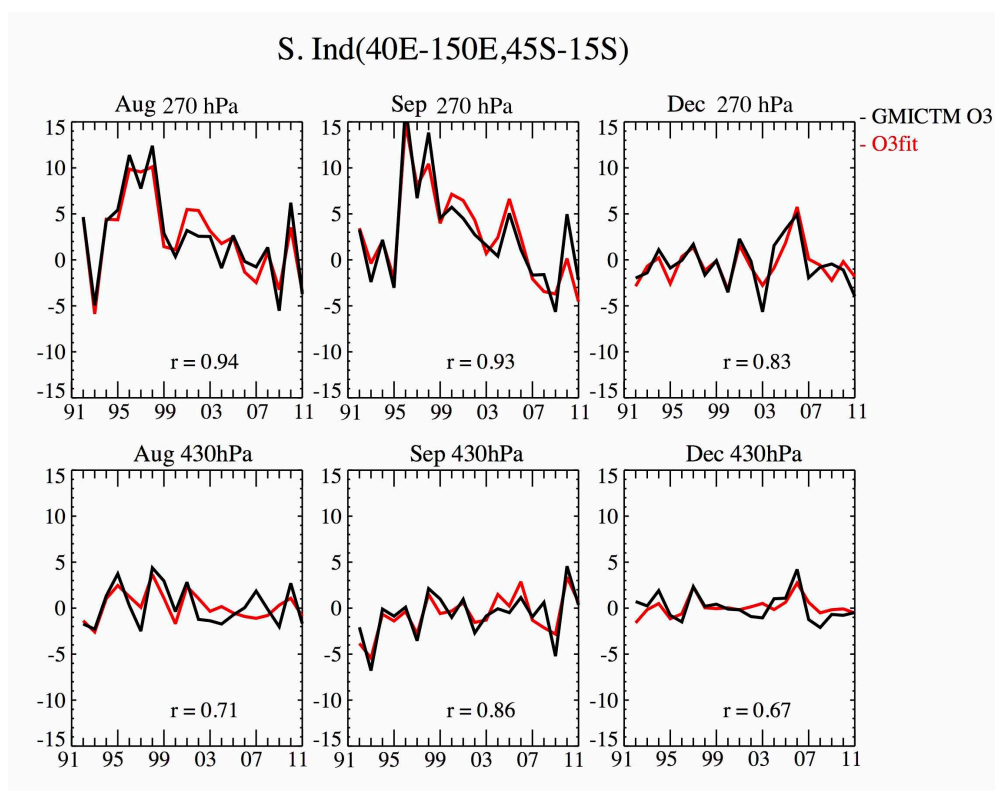
868



869

870

871 **Figure 8: The standardized anomalies of the tagged CO tracers over South Atlantic from three burning source**  
872 **regions, including southern Africa (red), South America (blue) and eastern region (green) and their comparison**  
**with the EmissO<sub>3</sub> (black) at 270 and 430 hPa in September and December from 1992 to 2011.**



873

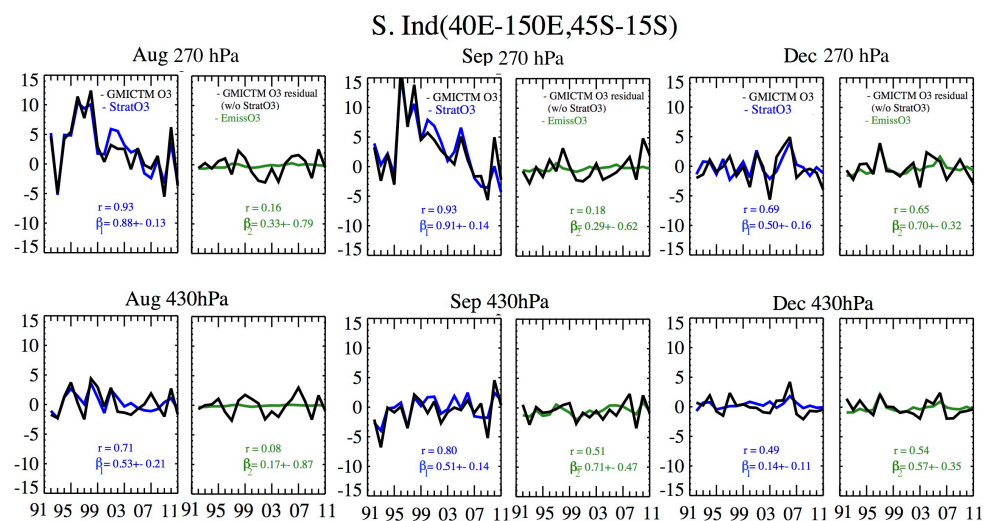
874

875

876

877

**Figure 9:** Comparison of the simulated ozone anomalies and the reconstructed ozone anomalies relying on two predictor variables: StratO<sub>3</sub>, EmissO<sub>3</sub> at 270 hPa and 430 hPa over South Indian Ocean region. Three panels show results from August (left), September (middle) and December (right) from 1992 to 2011. Unit for y-axis is ppb.



878

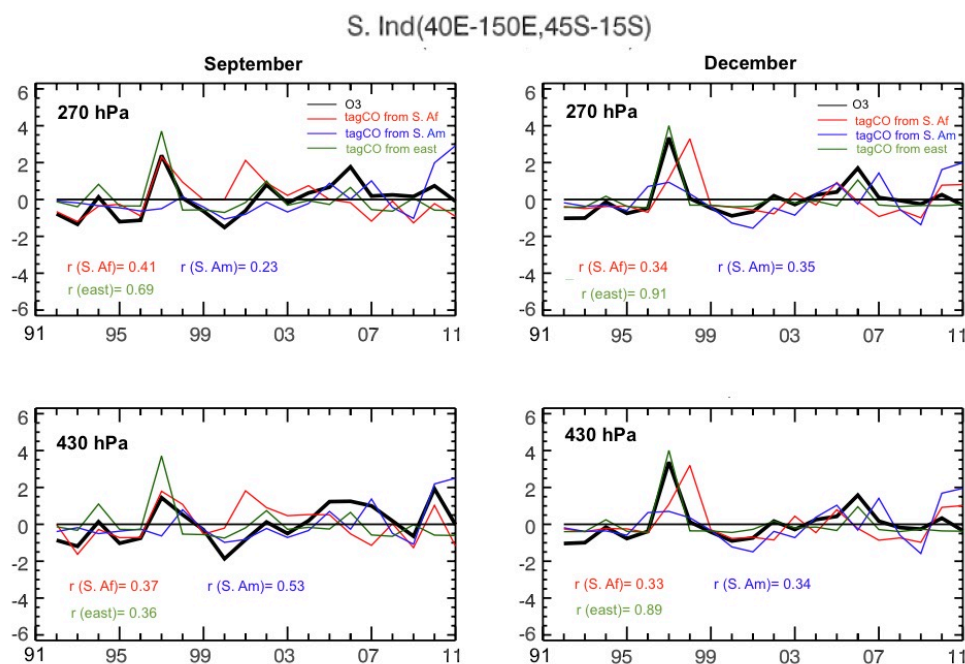
879

**Figure 10:** The multi-regression results of simulated ozone anomalies over South Indian Ocean region relying on two predictor variables: StratO<sub>3</sub> (blue), EmissO<sub>3</sub> (green) at 270 hPa and 430 hPa. Three panels show results from August (left), September (middle) and December (right) from 1992 to 2011. Each panel contains two columns. The left column of each panel compares the anomalies of StratO<sub>3</sub> (blue) and simulated ozone mixing ratio (black) from the GMI-CTM model at 270 and 430 hPa. The right column compares the simulated O<sub>3</sub> residual after removing the regression from StratO<sub>3</sub> (black line) and EmissO<sub>3</sub> (green line) at these two levels. EmissO<sub>3</sub> is calculated from the difference of simulated ozone between the run with yearly-varied emission and the run with constant emission. Unit for y-axis is ppb. The correlation (r), regression coefficient (β) and its 95% confidence level are labeled in each panel.

887



888



889

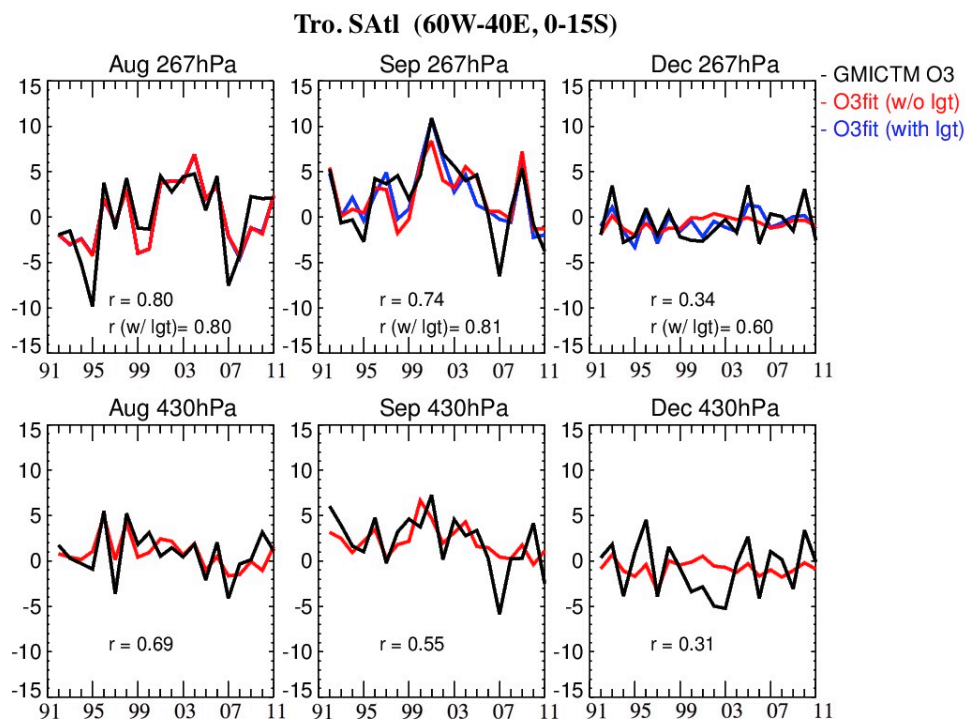
890

Figure 11: The standardized anomalies of the tagged CO tracers over South Indian Ocean region from three burning source regions, including southern Africa (red), South America (blue) and Eastern region (green) and their comparison with the EmissO<sub>3</sub> (black) at 270 and 430 hPa in September and December from 1992 to 2011.

891

892

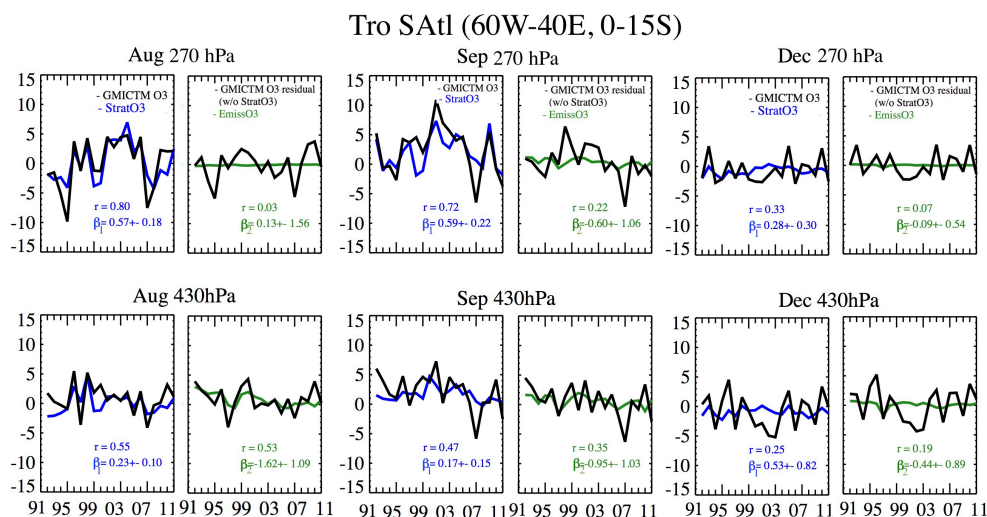
893



894

895

896 **Figure 12:** Comparison of the simulated ozone anomalies and the reconstructed ozone anomalies relying on two  
897 predictor variables: StratO<sub>3</sub>, EmissO<sub>3</sub> (red) over Tropical South Atlantic region at 270 hPa and 430 hPa. At 270  
898 hPa, the reconstructed ozone anomalies from three predictor variables including lightning NO<sub>x</sub> (blue) are  
899 added. Three panels show results from August (left), September (middle) and December (right) from 1992 to  
2011. Unit for y-axis is ppb.



900

901

**Figure 13:** The multi-regression results of simulated ozone anomalies over tropical South Atlantic region relying on StratO<sub>3</sub> (blue), EmissO<sub>3</sub> (green) at 270 hPa and 430 hPa. Three panels show results from August (left),

902

September (middle) and December (right) from 1992 to 2011. Each panel contains two columns. The left column

903

of each panel compares the anomalies of StratO<sub>3</sub> (blue) and simulated ozone mixing ratio (black) from the GMI-

904

CTM model at 270 and 430 hPa. The right column compares the simulated O<sub>3</sub> residual after removing the

905

regression from StratO<sub>3</sub> (black line) and EmissO<sub>3</sub> (green line) at these two levels. EmissO<sub>3</sub> is calculated from the

906

difference of simulated ozone between the run with yearly-varied emission and the run with constant emission.

907

Unit for y-axis is ppb. The correlation (r), regression coefficient (β) and its 95% confidence level are labeled in

908

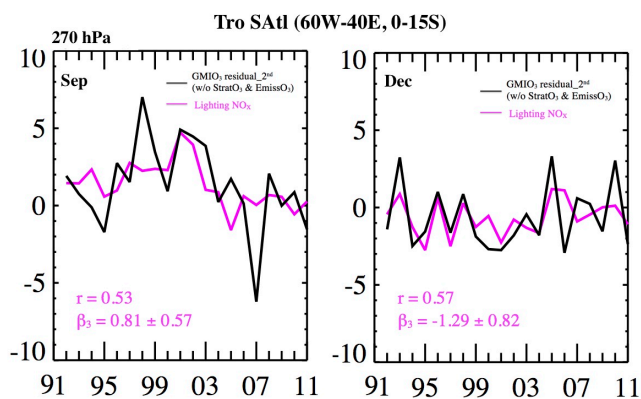
each panel

909

each panel



910



911

912

**Figure 14:** The comparison between regression of lightning NO<sub>x</sub> (magenta) and the ozone residual after removing the regression of StratO<sub>3</sub> and EmissO<sub>3</sub> (black) at 270 hPa in September (left) and December (right) over tropical South Atlantic region. The correlation ( $r$ ), regression coefficient ( $\beta$ ) and its 95% confidence level

913

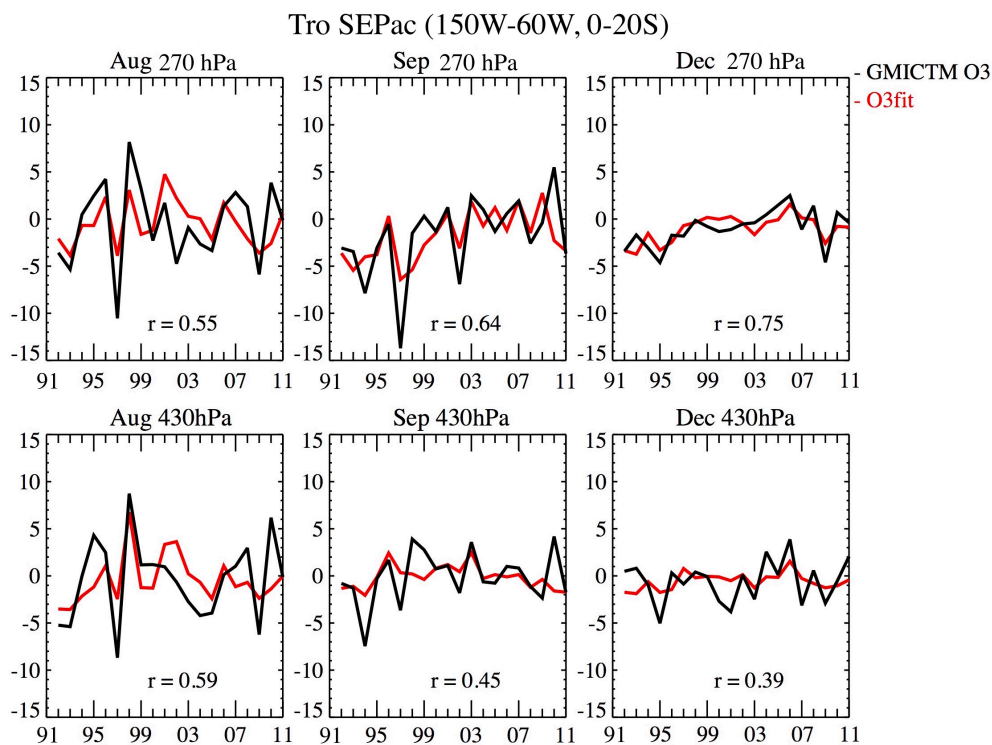
are labeled in each panel.

914

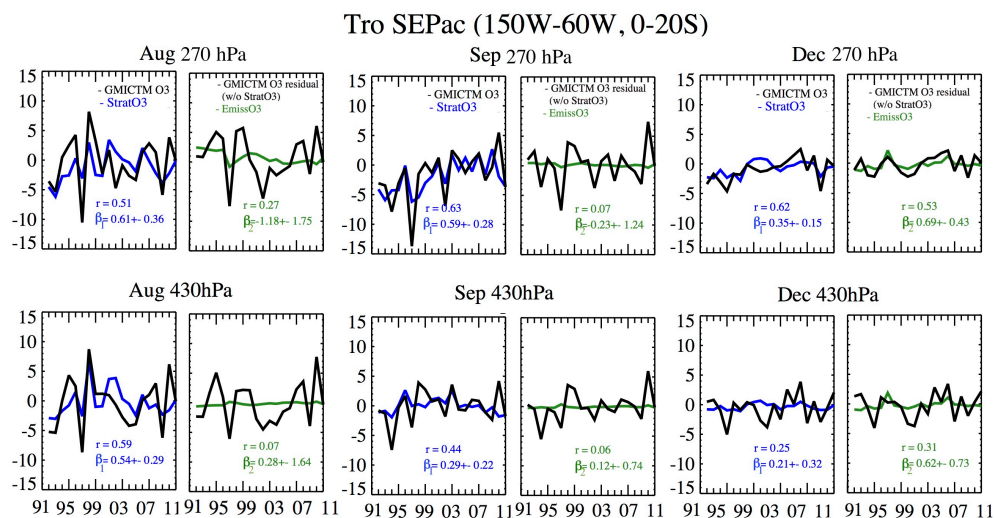
915

916

917



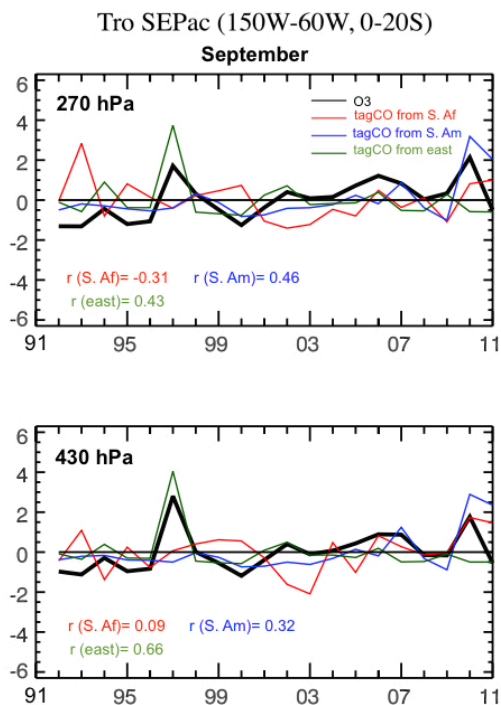
918  
919 **Figure 15:** Comparison of the simulated ozone anomalies and the reconstructed ozone anomalies relying on two  
920 predictor variables: StratO<sub>3</sub>, EmissO<sub>3</sub> at 270 hPa and 430 hPa over Tropical southeastern Pacific. Three panels  
921 show results from August (left), September (middle) and December (right) from 1992 to 2011. Unit for y-axis is  
922 ppb.



923

924

925 **Figure 16:** The multi-regression results of simulated ozone anomalies over tropical southeastern Pacific region  
 926 relying on two predictor variables: StratO<sub>3</sub> (blue), EmissO<sub>3</sub> (green) at 270 hPa and 430 hPa. Three panels show  
 927 results from August (left), September (middle) and December (right) from 1992 to 2011. Each panel contains  
 928 two columns. The left column of each panel compares the anomalies of StratO<sub>3</sub> (blue) and simulated ozone  
 929 mixing ratio (black) from the GMI-CTM model at 270 and 430 hPa. The right column compares the simulated  
 930 O<sub>3</sub> residual after removing the regression from StratO<sub>3</sub> (black line) and EmissO<sub>3</sub> (green line) at these two levels.  
 931 EmissO<sub>3</sub> is calculated from the difference of simulated ozone between the run with yearly-varied emission and  
 932 the run with constant emission. Unit for y-axis is ppb. The correlation (r), regression coefficient (β) and its 95%  
 confidence level are labeled in each panel.



933

934

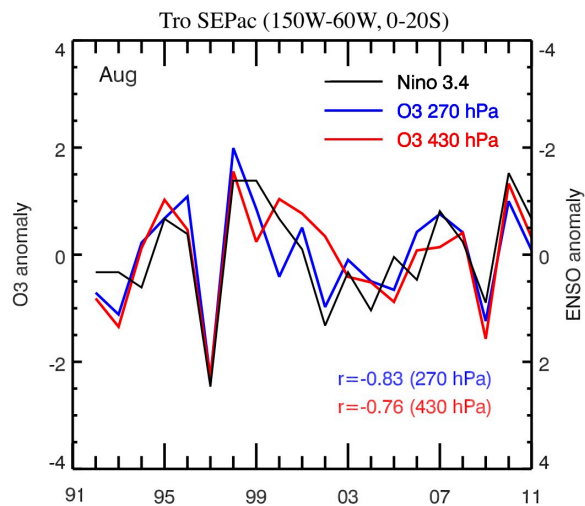
Figure 17: The standardized anomalies of the tagged CO tracers over tropical southeastern Pacific region from three burning regions, including southern Africa (red), South America (blue) and Eastern region (green) and their comparison with the EmissO3 (black) at 270 and 430 hPa in September from 1992 to 2011.

936

937

938

939



940

941

**Figure 18: Comparison of IAV of ozone anomalies over tropical southeastern Pacific region at 270 hPa (blue)**

942

**and 430 hPa (red) with Niño 3.4 index in August from 1992 to 2011. The 2<sup>nd</sup> y-axis for the ENSO anomaly is**

943

**reversed.**

944